On the simulation of cohesive fatigue effects in grain boundaries of a piezoelectric mesostructure

J. Utzinger [a,*], P. Steinmann [b], A. Menzel [c,d]

[a] *Lehrstuhl für Technische Mechanik, TU Kaiserslautern, P.O. Box 3049, D-67653 Kaiserslautern, Rheinland-Pfalz, Germany*
[b] *Lehrstuhl für Technische Mechanik, Universität Erlangen-Nürnberg, Egerlandstraße 5, D-91058 Erlangen, Germany*
[c] *Fachgebiet Mechanik, Insbesondere Maschinendynamik, TU Dortmund, Leonhard-Euler-Str. 5, D-44227 Dortmund, Germany*
[d] *Division of Solid Mechanics, Lund University, P.O. Box 118, SE-22100 Lund, Sweden*

ARTICLE INFO

ABSTRACT

Ferroelectric materials offer a variety of new applications in the field of smart structures and intelligent systems. Accordingly, the modelling of these materials constitutes an active field of research. A critical limitation of the performance of such materials is given when electrical, mechanical, or mixed loading fatigue occurs, combined with, for instance, microcracking phenomena. In this contribution, fatigue effects in ferroelectric materials are numerically investigated by utilisation of a cohesive-type approach. In view of finite element-based simulations, the geometry of a natural grain structure, as observed on the so-called meso-level, is represented by an appropriate mesh. While the response of the grains themselves is approximated by coupled continuum elements, grain boundaries are numerically incorporated via so-called cohesive-type or interface elements. These offer a great potential for numerical simulations: as an advantage, they do not result in bad-conditioned systems of equations as compared with the application of standard continuum elements inhering a very high ratio of length and height. The grain boundary behaviour is modelled by cohesive-type constitutive laws, designed to capture fatigue phenomena. Being a first attempt, switching effects are planned to be added to the grain model in the future. Two differently motivated fatigue evolution techniques are applied, the first being appropriate for low-cycle-fatigue, and a second one adequate to simulate high-cycle-fatigue. Subsequent to a demonstration of the theoretical and numerical framework, studies of benchmark boundary value problems with fatigue-motivated boundary conditions are presented.

© 2008 Elsevier Ltd. All rights reserved.

1. Introduction

In recent years, smart materials have occupied a decisive role in many fields of engineering science. They can be subdivided into several subclasses, e.g., piezoelectric solids, shape memory alloys, electro-rheostatic and magneto-rheostatic fluids, to name but a view. By their revolutionary properties, smart materials expand technical possibilities, in turn giving new inspiration to their own evolution. An apparent example is the continuing downsizing of the application scales, being documented by developments related to nanotechnology. Depending on the type of application, use can be made of both the

direct as well as the inverse piezoelectric effect. In any case, cyclic loading conditions are common, resulting in fatigue-related degradation of the various material properties.

Concerning fatigue life, many physical processes, occurring on different scales, are of interest. According to the literature, there are two types of fatigue, the first due to embrittlement and the second resulting from fatigue crack growth (Lupascu, 2004). In Daining et al. (2004) it was found for PZT, that for cyclic electric loading with an amplitude far below the coercitive field strength E_c, the evolution and propagation of parallel microcracks is observed. With the amplitude getting closer to E_c, macrocracks are emerging. Due to diffusion processes, the behaviour of piezoelectric materials is rate dependent (Lohkämper et al., 1990) and, consequently, fatigue effects are in general subject to cyclic frequency loading (Schorn et al., 2006). Dependent on the particular application considered, either low-cycle-fatigue or high-cycle-fatigue effects are observed. In this regard, geometrical influences as, e.g., notches (Westram et al., 2007), can lead to a very limited fatigue life. For electric loading, fatigue-related influences are highly concentrated at the electrodes. Certainly, in view of oscillating loading conditions close to some operating point near to the polarisation saturation, the high-cycle-loading type is most common. However, on the micro scale, domain switching within the grains, grain boundary effects and their interactions all together cause the fatigue properties of a piezoelectric material on the meso scale.

In this contribution, focus is placed on grain boundaries, amongst others being relevant when considering electrical properties of a piezoelectric ceramic (Knauer, 1982), and playing a crucial role in the fatigue behaviour (Lupascu, 2004). The smaller the grains are, the larger the influence of the grain boundaries on the global behaviour of the material becomes (Schaumburg, 1994). Consequently, grain boundaries are of crucial importance on the nano scale (Rühle, 2004,). They are mechanically weak (Lupascu, 2004) and reveal a lower permittivity than the grain bulk (Bast, 1985). Additionally, amorphous structures in the grain boundaries emerging under fatigue loading conditions (Lupascu, 2004) suggest very reduced coupling effects. According to Schaumburg (1994), driving forces for the defect structure of grain boundaries are the electrostatical potential, the degradation of elastic strain energy, and the formation of associated defects with dipole character.

To reduce the number of experiments, various simulation tools can be applied. Furthermore, by relating simulations and experimental results, further insight can be gained. In this context, the finite element-method makes a model of the mesostructure accessible to simulation. There are several proposals for thermodynamically motivated constitutive models for the bulk, e.g., Kamlah (2001), Kamlah and Böhle (2001), Schröder and Gross (2004), Schröder and Romanowski (2005), Klinkel (2006a), Klinkel (2006b) and Mehling et al. (2007), mostly incorporating switching phenomena, see also Arockiarajan et al. (2006), Arockiarajan and Menzel (2007), Menzel et al. (2008), and references cited therein. In view of finite element discretisations of polycrystalline mesostructures, it is well-established to generate appropriate meshes by utilisation of the Voronoi-tessellation (Espinosa and Zavattieri, 1999; Sfantos and Aliabadi, 2007). Additionally, though being restricted concerning its applications, the boundary-element-method can be applied to discretise grain boundaries (Sfantos and Aliabadi, 2007), thereby omitting the computational costs induced by discretised grains.

Grain boundaries are very narrow zones, being located in between surrounding grains. This suggests the application of so-called interface elements or cohesive-type elements to discretise grain boundaries. Interface elements are of one dimension smaller than surrounding continuum elements, thereby avoiding bad-conditioned stiffness matrices, as obtained for too narrow continuum elements (Schellekens and De Borst, 1993; Utzinger et al., 2007a). In this context, concerning the numerical modelling of interfaces, see also the approach based on regularised discontinuities by Jansson and Larsson (2001) and Larsson and Jansson (2002). To simulate grain boundaries in ceramics, Espinosa and Zavattieri (1999) incorporated a bilinear, irreversible cohesive law in an interfacial finite element context. Concerning fatigue damage, the reader is referred to the investigations by, e.g., Paas et al. (1993) and Peerlings et al. (2000). In these works, evolution criteria for non-piezoelectric bulk materials under cyclic loading are developed, especially suited for high-cycle-fatigue. Similar formulations have been proposed by Robinson et al. (2005), Munoz et al. (2006) and Erinc et al. (2007) for non-piezoelectric interfaces. A cohesive low-cycle-fatigue formalism was developed by Nguyen et al. (2001), and further extended by Arias et al. (2006) for coupled problems, however, without placing emphasis on its numerical implementation.

In this work, a polycrystalline mesostructure of PZT is discretised by triangular continuum elements for the grains and interface elements for the grain boundaries. The continuum material law is coupled and linear, while the interfacial material law is basically linear and decoupled, but endowed with a penalty formalism and two different fatigue damage evolutions. The first type is suitable for low-cycle-fatigue, while the second type captures high-cycle-fatigue. The constitutive model of the interface is artificial in nature, due to missing reliable information on the exact grain boundary behaviour for fatigue-type loading. It is designed to place emphasis on grain boundary effects and is believed to be a first step towards a sound physics-based model of real fatigue processes as, e.g., observed near the electrodes for electric loading. Both, switching and grain boundary effects, have to be considered in future works.

The paper is structured as follows: In Section 2, electromechanical field equations and thermodynamical relations are introduced. Related, residual quantities, namely stresses and dielectrical displacements, are derived. Moreover, the constitutive model of the bulk is exemplified. In Section 3, two different models for fatigue damage evolution are introduced. In detail, Section 3.1 deals explicitly with interfacial constitutive modelling details, concerning a so-called time-based fatigue formulation, being the appropriate choice for the simulation of low-cycle-fatigue. An interfacial constitutive model suitable for high-cycle-fatigue simulations is introduced in Section 3.2. Subsequently, Section 4 addresses finite element-related aspects with special emphasis on interface elements. A discretisation of a rectangular PZT mesostructure is introduced, serving as a framework for the implementation of the cohesive models examined before. Representative numerical results are presented in Section 5. Thereby, different low- and high-cycle-fatigue motivated boundary conditions are applied considering

both mechanical and electrical cycling. Subsequently, the results are discussed. Finally, conclusions and an outlook are given in Section 6.

In the following, brackets [•] denote mathematical groupings and intervals, parentheses (•) denote functional dependencies and curly brackets {•} are used in the context of sets. Double brackets $[\![\bullet]\!]$ denote a jump of some relevant argument, while the so-called Macaulay-brackets are defined as

$$\langle\bullet\rangle = \begin{cases} \bullet & \text{if} \quad \bullet > 0 \\ 0 & \text{if} \quad \bullet \leqslant 0 \end{cases} \tag{1}$$

2. Electrostatics

In this section, balance equations and thermodynamical considerations are reviewed, introducing the residual quantities of the bulk and the interface as stresses, or, respectively, tractions, and dielectrical displacements.

2.1. Balance equations

Let $\mathscr{B} \subseteq \mathbb{R}^{n_{\text{dim}}}$ be the configuration of a body of interest, subjected to small deformations. Then, position vectors pointing on $\mathscr{B}$ are denoted as $x \in \mathbb{R}^{n_{\text{dim}}}$ and related displacements and the electric potential shall be given as u and, respectively, Φ. Considering $\mathscr{B}$, inherent physical properties can be described as quasi-electrostatic and source-free, with body forces and external charges being neglected. Consequently, the local format of the balance of linear momentum reads as

$$\text{div}\boldsymbol{\sigma} = \mathbf{0} \quad \text{in} \quad \mathscr{B} \tag{2}$$

with $\boldsymbol{\sigma}$ being the stress tensor and boundary conditions

$$\boldsymbol{u} = \boldsymbol{u}_{\text{p}} \quad \text{on} \quad \partial\mathscr{B}_{\text{u}}, \quad \boldsymbol{\tau} = \boldsymbol{\sigma}\cdot\boldsymbol{n}_{\sigma} = \boldsymbol{\tau}_{\text{p}} \quad \text{on} \quad \partial\mathscr{B}_{\sigma} \tag{3}$$

Here, $\boldsymbol{\tau}_{\text{p}}$ are prescribed tractions and $\boldsymbol{n}_{\sigma}$ is the outward normal with respect to $\partial\mathscr{B}_{\sigma}$. For the present configuration, mechanical and electrical fluxes have to be considered. In this regard, the second balance law to be incorporated is the Gaussian law, resulting from Maxwell's equations, given as

$$\text{div}\boldsymbol{D} = 0 \quad \text{in} \quad \mathscr{B} \tag{4}$$

wherein $\boldsymbol{D}$ is the dielectrical displacement. Appropriate boundary conditions are given as

$$\Phi = \Phi_{\text{p}} \quad \text{on} \quad \partial\mathscr{B}_{\Phi}, \quad \Lambda = -\boldsymbol{D}\cdot\boldsymbol{n}_{D} = \Lambda_{\text{p}} \quad \text{on} \quad \partial\mathscr{B}_{D} \tag{5}$$

with Λ_{p} denoting external surface charges and $\boldsymbol{n}_{D}$ being the outward normal with respect to $\partial\mathscr{B}_{D}$, compare also Kamlah (2001) and Schröder and Romanowski (2005) or Maugin (1988) and Eringen and Maugin (1989). Without loss of generality, we restrict ourselves to a two-dimensional setting in the 1, 3-plane, i.e. $\mathscr{B} \subseteq \mathbb{R}^2$ which is splitted into two parts, denoted as $\mathscr{B}^+$ and $\mathscr{B}^-$. These are bonded by an interface, with Γ denoting the related centre line. Adequate interface-related position vectors $\boldsymbol{x}$ are only considered to point onto Γ. Furthermore, towards the interface, let $\mathscr{B}^+$ and $\mathscr{B}^-$ be closed by boundaries Γ^+ and Γ^-, see Fig. 1 for a visualisation. With respect to both $\mathscr{B}^+$ and $\mathscr{B}^-$, the before mentioned balance equations retain all their validity. Additionally, a traction equilibrium condition, incorporating Cauchy's lemma and theorem, reads as

$$\boldsymbol{\tau}_{\Gamma^+} + \boldsymbol{\tau}_{\Gamma^-} = \mathbf{0}, \quad \text{with} \quad \boldsymbol{\tau}_{\Gamma^+} = \boldsymbol{\sigma}\cdot\boldsymbol{n}_{\Gamma^+}, \quad \boldsymbol{\tau}_{\Gamma^-} = \boldsymbol{\sigma}\cdot\boldsymbol{n}_{\Gamma^-} \tag{6}$$

see also Fig. 1 for further explanation, and a displacement compatibility condition is given as

$$\boldsymbol{u}_{\Gamma^+} - \boldsymbol{u}_{\Gamma^-} = [\![\boldsymbol{u}]\!] \tag{7}$$

Furthermore, a dielectrical displacement equilibrium condition takes the representation
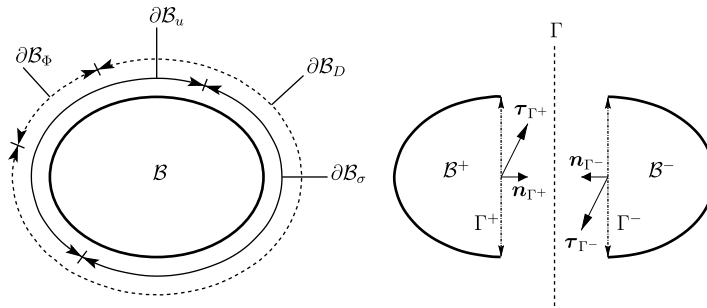

Fig. 1. Configuration $\mathscr{B}$, interface Γ, some boundary and complementing conditions.

$$\Lambda_{\Gamma^+} + \Lambda_{\Gamma^-} = 0, \quad \text{with} \quad \Lambda_{\Gamma^+} = -\boldsymbol{D} \cdot \boldsymbol{n}_{\Gamma^+}, \quad \Lambda_{\Gamma^-} = -\boldsymbol{D} \cdot \boldsymbol{n}_{\Gamma^-} \tag{8}$$

while the electric potential compatibility condition reads as

$$\Phi_{\Gamma^+} - \Phi_{\Gamma^-} = [\![\Phi]\!] \tag{9}$$

2.2. Electric enthalpy of the bulk and related residual quantities

In order to concentrate on grain boundary effects, a linear coupled material law is incorporated for the bulk. Accordingly, an operating point close to a saturated polarisation is assumed and switching effects are neglected. Furthermore, any rate dependencies are excluded. Consequently, the electric enthalpy of the bulk can be specified as

$$H^{\diamond}(\boldsymbol{\varepsilon}, \boldsymbol{E}) = \inf_{\boldsymbol{D}}(\Psi^{\diamond} - \boldsymbol{E} \cdot \boldsymbol{D}) = \frac{1}{2}\boldsymbol{\varepsilon} : \boldsymbol{C}^{\diamond} : \boldsymbol{\varepsilon} - \boldsymbol{E} \cdot \boldsymbol{e}^{\diamond} : \boldsymbol{\varepsilon} - \frac{1}{2}\boldsymbol{E} \cdot \boldsymbol{\epsilon}^{\diamond} \cdot \boldsymbol{E} \tag{10}$$

compare also Schröder and Gross (2004) or the textbook of Smith (2005), with index $\diamond$ denoting bulk quantities, see Table 1. Here, the electric enthalpy $H^{\diamond}$ is summarising a mechanical part, a coupling part, and a purely electrical part. The transversely isotropic stiffness tensor, reflecting the underlying tetragonal symmetry, can be described in Voigt notation (index V), given as

$$[\boldsymbol{C}^{\diamond}]_{ij}^{V} = \begin{bmatrix} \lambda + 2\mu_{\perp} & \lambda + \zeta & 0 \\ \lambda + \zeta & \lambda + 2\zeta + \eta - 2\mu_{\perp} + 4\mu_{\parallel} & 0 \\ 0 & 0 & \mu_{\parallel} \end{bmatrix} \tag{11}$$

with elastic constants λ, $\mu_{\perp}$, $\mu_{\parallel}$, ζ, and η. The Voigt-notated matrix of piezoelectric coefficients is given as

$$[\boldsymbol{e}^{\diamond}]_{ij}^{V} = \begin{bmatrix} 0 & e_{31} \\ 0 & e_{33} \\ e_{15} & 0 \end{bmatrix} \tag{12}$$

while the permittivity matrix reads as

$$[\boldsymbol{\epsilon}^{\diamond}]_{ij} = \begin{bmatrix} \epsilon_{11} & 0 \\ 0 & \epsilon_{33} \end{bmatrix} \tag{13}$$

The appropriate dissipation inequality, or, respectively, Clausius–Duhem inequality is conforming to the electric enthalpy-based Clausius–Planck inequality. It is given by means of the stress power $\mathscr{W}_{\text{mech}}^{\diamond}$, the complementary dielectric displacement power $\mathscr{W}_{\text{elec}}^{\diamond,*}$, and the rate of the bulk electric enthalpy $\dot{H}^{\diamond}$ as

$$\mathscr{D}^{\diamond} = \mathscr{D}_{\text{loc}}^{\diamond} = \mathscr{W}_{\text{mech}}^{\diamond} - \mathscr{W}_{\text{elec}}^{\diamond,*} - \dot{H}^{\diamond} = \boldsymbol{\sigma} : \dot{\boldsymbol{\varepsilon}} - \boldsymbol{D} \cdot \dot{\boldsymbol{E}} - \dot{H}^{\diamond} \geqslant 0 \tag{14}$$

which is equivalent to

$$\left[\boldsymbol{\sigma} - \frac{\partial H^{\diamond}}{\partial \boldsymbol{\varepsilon}}\right] : \dot{\boldsymbol{\varepsilon}} + \left[-\boldsymbol{D} - \frac{\partial H^{\diamond}}{\partial \boldsymbol{E}}\right] \cdot \dot{\boldsymbol{E}} \geqslant 0 \tag{15}$$

The Coleman–Noll entropy principle then directly implies the residual quantities of stresses and dielectrical displacements to be given as the derivatives of the electric enthalpy with respect to the strain tensor and the electric field vector. Accordingly, the stress tensor takes the representation

$$\boldsymbol{\sigma} = \partial_{\boldsymbol{\varepsilon}} H^{\diamond} = \boldsymbol{C}^{\diamond} : \boldsymbol{\varepsilon} - \boldsymbol{e}^{\diamond} \cdot \boldsymbol{E} \tag{16}$$

while the dielectric displacement vector reads as

$$\boldsymbol{D} = -\partial_{\boldsymbol{E}} H^{\diamond} = \boldsymbol{e}^{\diamond} : \boldsymbol{\varepsilon} + \boldsymbol{\epsilon}^{\diamond} \cdot \boldsymbol{E} \tag{17}$$

Table 1
Quantities occurring in the electric enthalpy formulation of the bulk

$\boldsymbol{\varepsilon} = \nabla^{\text{sym}}\boldsymbol{u}$	Strain tensor
$\boldsymbol{u}$	Displacement vector
$\boldsymbol{E} = -\nabla\Phi$	Electric field vector
Φ	Electric potential
$\boldsymbol{D}$	Dielectric displacement vector
$\Psi^{\diamond}$	Free energy
$\boldsymbol{C}^{\diamond}$	Transversely isotropic elastic stiffness tensor
$\boldsymbol{e}^{\diamond}$	Piezoelectric coefficient tensor
$\boldsymbol{\epsilon}^{\diamond}$	Permittivity tensor

Consequently, the reduced format of the Clausius–Planck inequality

$$\mathscr{D}_{\mathrm{red}}^{\diamond} = 0 \geqslant 0 \tag{18}$$

is trivially satisfied, with any dissipative effects in the bulk material being excluded.

2.3. Electric enthalpy of the interface and related residual quantities

In view of the grain boundaries, or rather interfaces, the quantities of displacements and electric potential are replaced by jump quantities over the interface, i.e. the displacement jump and the electric potential jump, due to reasons exposed in the introduction. The starting point for the subsequent elaborations is a linear, coupled interfacial material behaviour. For grain boundaries associated with the centre line Γ of an interface, opposite surface lines are identified with Γ^{+} and Γ^{-}. As a penetration of the opposite surface lines should be avoided for obvious physical reasons, an adequate penalty formalism has additionally to be considered to guarantee

$$[\![\boldsymbol{u}(\boldsymbol{x})]\!] \cdot \boldsymbol{n}_{\Gamma^{-}} \geqslant 0 \quad \forall \quad \boldsymbol{x} \in \Gamma \tag{19}$$

Furthermore, to account for fatigue effects, a change of constitutive tensors is incorporated in the subsequent elaborations. This is accomplished by introducing a damage parameter

$$d \in [0, 1] \tag{20}$$

In grain boundaries, foreign atoms and impurities are deposited, not fitting into the stable crystal configuration of the grains. Additionally, secondary phases can occur (Schaumburg, 1994), resulting in a more or less heterogeneous consistency. As already mentioned, amorphous structures in the grain boundaries emerge under fatigue loading conditions. Based on these informations, a piezoelectric coupling mechanism is considered to be of a very reduced intensity. Consequently, the interfacial coupling factor will be set to zero. Depending on certain doping conditions, grain boundaries might become highly charged interface layers (Lupascu, 2004). In this case, capacitor-type interfacial material laws could be applied, which constitutes current and future research.

Taking into account the constitutive characteristics highlighted above, an electric enthalpy for the interface shall be introduced as

$$H([\![\boldsymbol{u}]\!], E) = \inf_{A}(\Psi - E\Lambda) = \frac{1}{2}[1 - d][\![\boldsymbol{u}]\!] \cdot \boldsymbol{C} \cdot [\![\boldsymbol{u}]\!] - \frac{1}{2}\epsilon_0 \epsilon_r(d) E^2 + \frac{q}{6} \langle -[\![\boldsymbol{u}]\!] \cdot \boldsymbol{n} \rangle^3 \tag{21}$$

with the quantities incorporated being defined in Table 2. Please note that as this work proceeds, we identify $\boldsymbol{n} = \boldsymbol{n}_{\Gamma^{-}}$. The interfacial electric enthalpy H is composed of a mechanical part, an electrical part and a penalty part. In this context, the electric enthalpy-based Clausius–Duhem inequality, or rather Clausius–Planck inequality, is determined by means of the interfacial stress power $\mathscr{W}_{\mathrm{mech}}$, the interfacial complementary dielectric displacement power $\mathscr{W}_{\mathrm{elec}}^{*}$, and the rate of the interfacial electric enthalpy $\dot{H}$, namely

$$\mathscr{D} = \mathscr{D}_{\mathrm{loc}} = \mathscr{W}_{\mathrm{mech}} - \mathscr{W}_{\mathrm{elec}}^{*} - \dot{H} = \boldsymbol{\tau} \cdot [\![\dot{\boldsymbol{u}}]\!] - \Lambda\dot{E} - \dot{H} \geqslant 0 \tag{22}$$

which is equivalent to

$$\left[\boldsymbol{\tau} - \frac{\partial H}{\partial[\![\boldsymbol{u}]\!]}\right] \cdot [\![\dot{\boldsymbol{u}}]\!] + \left[-\Lambda - \frac{\partial H}{E}\right]\dot{E} - \frac{\partial H}{\partial d}\dot{d} \geqslant 0 \tag{23}$$

and, considering the Coleman–Noll entropy principle, renders the residual quantities of the interface as derivatives of the interfacial electric enthalpy. Straightforwardly, the traction vector follows as:

$$\boldsymbol{\tau} = \partial_{[\![\boldsymbol{u}]\!]}H = [1 - d]\boldsymbol{C} \cdot [\![\boldsymbol{u}]\!] - \frac{q}{2}\langle -[\![\boldsymbol{u}]\!] \cdot \boldsymbol{n} \rangle^2 \boldsymbol{n} \tag{24}$$

Table 2
Quantities occurring in the electric enthalpy formulation of the interface

$[\![\boldsymbol{u}]\!]$	Displacement jump
$E = -[\![\Phi]\!]$	Electric field
$[\![\Phi]\!]$	Electric potential jump
Ψ	Free energy in the interface
Λ	Dielectric displacement
d	Damage variable
$\boldsymbol{C} = c_s\boldsymbol{s} \otimes \boldsymbol{s} + c_n\boldsymbol{n} \otimes \boldsymbol{n}$	Elastic stiffness tensor
c_s, c_n	Stiffness parameters
$\{\boldsymbol{s}, \boldsymbol{n}\}$	Interfacial orthonormal base system
ϵ_0	Permittivity of the vacuum
$\epsilon_r(d)$	Relative permittivity
$q > 0$	Penalty stiffness

Similar to considerations that fatigue loading conditions weaken the grain boundary bonds (Lupascu, 2004), interfacial tractions are reduced by application of the above parameter d in the context of Lemaitre-type damage, if the driving force allows. The dielectric displacement is derived as

$$\Lambda = -\partial_E H = \epsilon_0 \epsilon_r(d) E \tag{25}$$

The reduced format of the Clausius–Planck inequality follows as

$$\mathscr{D}_{\text{red}} = -\frac{\partial H}{\partial d} \dot{d} = \left[\frac{1}{2} \llbracket \boldsymbol{u} \rrbracket \cdot \boldsymbol{C} \cdot \llbracket \boldsymbol{u} \rrbracket + \frac{1}{2} \epsilon_0 E^2 \frac{\partial \epsilon_r(d)}{\partial d} \right] \dot{d} = Y \dot{d} \geqslant 0 \tag{26}$$

whereby the driving force is identified with Y. Here, healing processes of the damage are excluded. Consequently, the rate of the damage parameter is constrained by

$$\dot{d} \geqslant 0 \tag{27}$$

Due to the fact that the driving force constrains the kinetics of the damage parameter evolution, inequalities (26) and (27) indicate

$$\dot{d} > 0 \quad \text{for} \quad Y > 0 \tag{28}$$

$$\dot{d} = 0 \quad \text{for} \quad Y \leqslant 0 \tag{29}$$

For the issue of Lemaitre-type damage, see also Lemaitre (1994), Lemaitre and Chaboche (1994), Menzel and Steinmann (2001), Ekh et al. (2003) and Willam et al. (2004). Moreover, it has been assumed that the interfacial permittivity $\epsilon = \epsilon_0 \epsilon_r(d)$ is also subject to fatigue effects.

2.4. Modelling of the permittivity change

From the experimental point of view, it could not yet been clarified how the grain boundary permittivity changes under fatigue loading conditions. The permittivity is defined as the polarisation capability of a medium. An argument for a decreasing permittivity could be that given dipolar structures are destroyed by some kind of fatigue-related erosion, or that the intergranular medium is endowed with, e.g., oxygen vacancies, eventually diffusing out of the bulk under fatigue loading (Lupascu, 2004). In view of the permittivity-decreasing influence of cracks, the present model only accounts for a very reduced broadening of grain boundaries. Concerning the phenomenon of microcracking, it is not yet fully understood and still subject of intense discussion, see Lupascu (2004) and references cited therein. Moreover, shaking and aligning of ions due to fatigue loading conditions, as well as some hypothetical increase of the ion concentration in the grain boundary due to cyclic loading, would suggest an increasing permittivity. Certainly, concerning the thermodynamically motivated considerations of the above, simplified assumptions have been made. Chemical potentials as well as any fluxes, diffusion phenomena or dipolar charges are neglected, but for sure play a role and consequently motivate further research and enhanced modelling approaches. Up to now, the rather simple free energy-motivated approach being applied here reflects a first attempt that has to be extended towards more sophisticated and physical sound models. Due to the unclear physical circumstances, an artificial but simple linear relation concerning the permittivity is assumed as

$$\epsilon_r(d) = \left[\epsilon_r^{\text{init}} + [\epsilon_r^{\text{end}} - \epsilon_r^{\text{init}}] d \right] \tag{30}$$

Here, ϵ_r^{init} denotes the relative permittivity at the beginning of a damaging process, while ϵ_r^{end} is the relative permittivity at the end when $d = 1$.

3. Fatigue damage evolution

In the following, two differently motivated fatigue damage evolution formulations are presented. The first one is called "time-based fatigue formulation" and is appropriate for low-cycle-fatigue simulations, while the second one, named "cycle-based fatigue formulation", is capable of representing high-cycle-fatigue loadings. Both methods inhere a common ground which is given by an effective quantity δ, defined as

$$\delta = \sqrt{\beta_s^2 \llbracket u_s \rrbracket^2 + \beta_n^2 \llbracket u_n \rrbracket^2 + \beta_\Phi^2 \llbracket \Phi \rrbracket^2} \tag{31}$$

with

$$\llbracket u_s \rrbracket = \llbracket \boldsymbol{u} \rrbracket \cdot \boldsymbol{s}, \quad \llbracket u_n \rrbracket = \llbracket \boldsymbol{u} \rrbracket \cdot \boldsymbol{n} \tag{32}$$

and β_s, β_n, and β_Φ denoting material parameters, controlling the influence of the projected displacement jumps and the electric potential jump on δ, while s and n are orthonormal unit vectors characterising the interface itself, compare Fig. 4. Grain boundary physics is not fully understood yet, but in order to take into account the influence of both the displacement and the electric potential, this rather simplified approach is applied. Without taking notice of the potential jump, it has intensively been used in the literature, see e.g., Pandolfi and Ortiz (1998), Pandolfi et al. (1999), Ortiz and Pandolfi (1999), Cirak et al.

(2005), Corigliano et al., 2006, and others. It has been expanded by Arias et al. (2006), incorporating the electric potential jump into the effective quantity.

3.1. Time-based fatigue formulation

The fatigue formulation introduced in this section is called time-based, because it can trace a cyclic loading history not in cycle-by-cycle steps, but in arbitrarily exact time intervals, or, respectively, loading segments. One of the first publications concerning this matter, considering an unloading–reloading hysteresis for a traction–separation correlation, is Nguyen et al. (2001). Therein, loading stiffness rates have been constructed such that shakedown effects are prevented. An application to the prediction of fatigue crack nucleation has been provided by Serebrinsky and Ortiz (2005), while Arias et al. (2006) applied the same elaborations to the cohesive modelling of ferroelectric fatigue. Depending on certain circumstances, e.g., geometrical influences like notches, low-cycle-fatigue occurs, see for example Westram et al. (2007).

The material law which is applied to capture low-cycle-fatigue is given as an exponential function, to be specific

$$d = \exp\left(-\frac{\alpha}{\tilde{\delta}}\right) \quad \Rightarrow d \in [0, 1) \tag{33}$$

with α being a positive material parameter. $\tilde{\delta}$ takes the interpretation as a history-dependent effective quantity. An incremental update for the damage variable is then accomplished, with index $n + 1$ denoting the current loading step. It is given as

$$d_{n+1} = \exp\left(-\frac{\alpha}{\tilde{\delta}_{n+1}}\right) \tag{34}$$

The related history-dependent effective quantity $\tilde{\delta}$ is updated as follows:

$$\tilde{\delta}_{n+1} = \tilde{\delta}_n + \langle \delta_{n+1} - \delta_n \rangle, \quad \tilde{\delta}_0 = 0 \tag{35}$$

The sketch of Fig. 2 schematically illustrates the effective quantity δ and the projection of the traction vector τ onto the interfacial normal vector $\boldsymbol{n}$ for some cyclic loading boundary conditions. For loading, the expression in the Macaulay-brackets is positive and the history-dependent effective quantity is updated, whereas, for unloading, it will be retained. In Fig. 2, points of time where loading passes into unloading are marked by a circle. Consequently, only an increasing δ contributes to the damage evolution in this rather simple, but efficient formulation. Nevertheless, all types of cycling, incorporating cyclic compressive, tensile and alternating loads, are time-explicitly reflected, contributing to the evolution of d in the same manner.

3.2. Cycle-based fatigue formulation

In this section, a fatigue formulation for high-cycle-fatigue is introduced. It is based on a constitutive integration over many cycles by means of a cycle number N. This idea has first been implemented for continua by Paas et al. (1993) and Peerlings et al. (2000). Concerning interfaces, similar formulations have been adopted for uncoupled problems by Robinson et al. (2005), Munoz et al. (2006) and Erinc et al. (2007). In the following, we will proceed along the strategy described in Peerlings et al. (2000). The damage variable is related to the deformation by means of a damage loading function
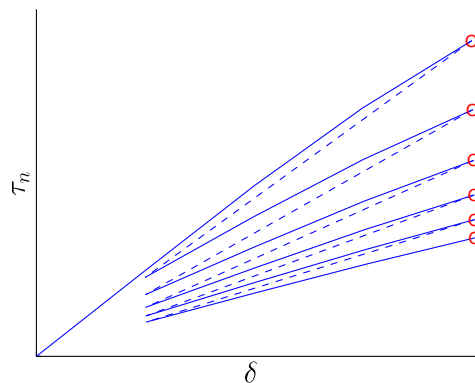

Fig. 2. Schematic sketch of the normal traction component over the effective quantity, using the update from Eqs. (34) and (35). The solid line indicates loading, whereas the dotted line denotes unloading.

$$f(\delta, \kappa) = \delta - \kappa \tag{36}$$

where κ is a threshold. Thereby, damage evolution will be active if the given effective quantity δ exceeds κ. Here, the material law is given by the rate of the damage parameter d as

$$\dot{d} = \begin{cases} h(d, \delta)\dot{\delta} & \text{if} \quad f \geqslant 0 \quad \text{and} \quad \dot{f} \geqslant 0 \quad \text{and} \quad d < 1 \\ 0 & \text{else} \end{cases} \tag{37}$$

with the evolution function

$$h(d, \delta) = C \exp(\gamma d)\delta^{\beta} \tag{38}$$

and C, β, and γ denoting material parameters. Now, assume d_t, $d_{t+\Delta t}$ to be damage parameters corresponding to points in time t and $t + \Delta t$. For continued loading, integration of Eq. (37) then renders

$$d_{t+\Delta t} = d_t + \int_t^{t+\Delta t} \dot{d}(\tau)\mathrm{d}\tau \tag{39}$$

To avoid the influence of some highly varying $\dot{d}$, an approximation of this correlation is not advisable. Therefore, a sum notation with respect to single cycles in combination with a transformation of integration limits concerning time and cycle numbers is accomplished. With this in hand and the damage evolution being active, combining Eqs. (37) and (39) renders

$$d_{N+\Delta N} = d_N + \sum_{k=N}^{N+\Delta N} \int_\kappa^{\delta_{a,k}} h(d_k, \delta_k)\mathrm{d}\delta_k \tag{40}$$

with N and $N + \Delta N$ being the number of performed cycles at points in time t and $t + \Delta t$. Moreover, $\delta_{a,k}$, δ_k, and d_k denote the effective parameter amplitude at cycle k, the variable effective parameter and damage parameter during cycle k. It shall be mentioned that, again, only loading related δ shall contribute to the damage evolution. For the thus obtained expression for $d_{N+\Delta N}$, neither $\delta_{a,k}$ nor d_k would vary much within a sufficiently small increment ΔN. Hence, the sum expression in Eq. (40) can now be approximated. Application of the trapezoidal rule with respect to loading cycles N and $N + \Delta N$ is reasonable, which ends up with

$$d_{N+\Delta N} = d_N + \frac{1}{2}[\mathscr{H}(d_N, \delta_{a,N}) + \mathscr{H}(d_{N+\Delta N}, \delta_{a,N+\Delta N})]\Delta N \tag{41}$$

wherein

$$\mathscr{H} = \begin{cases} \int_\kappa^{\delta_a} h(d, \delta)\mathrm{d}\delta & \text{if} \quad \delta_a > \kappa \\ 0 & \text{else} \end{cases} \tag{42}$$

Next, according to Peerlings et al. (2000), Heun's method enables to solve Eq. (41). This is accomplished by incorporating the Euler forward method. In detail, introducing a predictor value d_p, reading as

$$d_p = d_N + \mathscr{H}(d_N, \delta_{a,N})\Delta N \tag{43}$$

replaces $d_{N+\Delta N}$. Finally, Eq. (41) together with (43) render the damage update to take the format

$$d_{N+\Delta N} = d_N + \frac{1}{2}[\mathscr{H}(d_N, \delta_{a,N}) + \mathscr{H}(d_p, \delta_{a,N+\Delta N})]\Delta N \tag{44}$$

which nicely can be incorporated into a finite element context. The accuracy of this strategy is raised by diminishing ΔN. For $\kappa \neq 0$, either the range of cyclic compressive or tensile loads can be addressed, or a non-damaging regime concerning δ is achieved for cyclic alternating loads. Additionally, a so-called damage cut-off is defined via

$$d_{N+\Delta N} = 0.99 \quad \text{if} \quad d_N + \frac{1}{2}[\mathscr{H}(d_N, \delta_{a,N}) + \mathscr{H}(d_p, \delta_{a,N+\Delta N})]\Delta N > 0.99 \tag{45}$$

4. Finite element formulation

Embedded between standard continuum elements, interface elements have no numerical width. They are designed to model material interfaces and do not possess typical deficiencies (as for instance bad-conditioned tangent operators) of continuum elements with a very high ratio of length and height. In this work, grain boundaries are identified as a-priori-known zones of delamination. Hence, combined with appropriate constitutive models, interface elements can systematically be used to model intergranular weak zones.

In the following, a PZT polycrystalline mesostructure is discretised with finite elements. At first, a motivating micrograph of a specimen of the mentioned functional ceramic is highlighted, together with an appropriate FE-discretisation. Subsequently, detailed remarks on, e.g., weak forms, interface elements, and linearisation are provided. All considerations are reviewed for a two-dimensional problem.

4.1. Discretisation

To enlighten the functionality of the fatigue-related material laws of the above, a piezoelectric mesostructure, imported from Nuffer et al. (2000), is discretised with finite elements. In a non-linear finite element algorithm, low- and high-cycle-fatigue related constitutive relations are reflected by means of algorithmic tangent moduli. Thereafter, the finite element model can be subjected to different low- and high-cycle-fatigue-motivated boundary conditions. The present mesostructure, shown in Fig. 3 on the left hand side, is a micrograph of PIC 151, manufactured by PI Ceramic, Lederhose, Germany. It has been generated by a scanning electron microscope (SEM). PIC 151 is a standard material for actuators and suitable for low-power ultrasonic transducers and low-frequency sound transducers. On the right hand side of Fig. 3, an adequate discretisation of this mesostructure is highlighted. Grains are represented by continuum elements, and red-coloured. A pragmatic choice are linear triangular elements, geometrically defined by some point inside the grain and the grain polygon. The dark-blue-coloured interface elements are given at every grain boundary as one side of the related grain polygons, whereby each interface element is surrounded by two triangular elements. In this two-dimensional approximation of a real mesostructure, concerning the micrograph on the left hand side of Fig. 3, surfaces of underlying grains, apparent as black areas, are treated as voids in the related discretisation, see the right hand side of Fig. 3.

4.2. Global level

For the given coupled problem, the displacements $\boldsymbol{u}$ and the electric potential Φ are considered to contribute to the virtual work representation by means of their virtual counterparts. These can be interpreted as displacement test functions $\boldsymbol{\alpha}$ and electric potential test functions β. The principle of virtual work renders two weak equations, one related to the balance of linear momentum, the other reflecting the Gaussian law, namely

$$G_{\boldsymbol{u}} = \int_{B \backslash \Gamma} \varepsilon(\boldsymbol{\alpha}) : \boldsymbol{\sigma}(\boldsymbol{u}, \Phi) \mathrm{d}A + \int_{\Gamma} [\![\boldsymbol{\alpha}]\!] \cdot \boldsymbol{\tau}([\![\boldsymbol{u}]\!], [\![\Phi]\!]) \mathrm{d}S - \int_{\partial \mathscr{B}_{\sigma}} \boldsymbol{\alpha} \cdot \boldsymbol{\tau}_{\mathrm{p}} \mathrm{d}S = 0 \quad \text{and} \quad \boldsymbol{u} = \boldsymbol{u}_{\mathrm{p}} \quad \text{on} \quad \partial \mathscr{B}_{u} \tag{46}$$

$$G_{\Phi} = \int_{B \backslash \Gamma} \boldsymbol{E}(\beta) \cdot \boldsymbol{D}(\boldsymbol{u}, \Phi) \mathrm{d}A + \int_{\Gamma} E(\beta) \Lambda([\![\boldsymbol{u}]\!], [\![\Phi]\!]) \mathrm{d}S + \int_{\partial \mathscr{B}_{D}} \beta \, q_{\mathrm{p}} \mathrm{d}S = 0 \quad \text{and} \quad \Phi = \Phi_{\mathrm{p}} \quad \text{on} \quad \partial \mathscr{B}_{\Phi} \tag{47}$$

Within Eqs. (46) and (47), integration areas are separated with respect to the bulk, denoted as $\mathscr{B}$, the bulk Neumann boundaries $\partial \mathscr{B}_{\sigma}$ and $\partial \mathscr{B}_{D}$, and the interface, identified with Γ. Corresponding infinitesimal area and line elements are denoted as dA and dS.
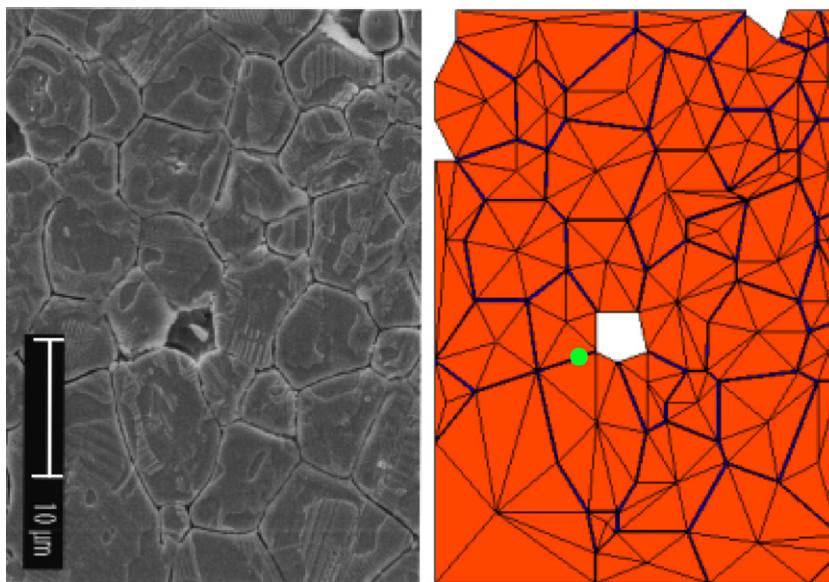

Fig. 3. Micrograph of PIC 151 (left, courtesy by Prof. D.C. Lupascu, see Nuffer et al. (2000)) and finite element discretisation (right). Continuum elements are coloured red, interface elements are dark blue. The green spot marks the Gauss point where the damage variables for Figs. 23 and 24 are saved. (For interpretation of the references to colour in this figure legend, the reader is referred to the web version of the article.)

4.3. Interface element level

Next, emphasis is placed on elaborations on the interface element level. In our case, linear line interface elements are applied, generally being surrounded by two linear triangular elements, see Fig. 4 for a graphical illustration. The energetically conjugate quantities of the interface are tractions τ and relative displacement jumps $[\![\boldsymbol{u}]\!]$, and, respectively, dielectric displacements $\varLambda$ and electric potential jumps $[\![\varPhi]\!]$. To include those jumps within a finite element context, the dependencies of $[\![\boldsymbol{u}]\!]$ and $[\![\varPhi]\!]$ on absolute degrees of freedom $\boldsymbol{u}$ and $\varPhi$ must be incorporated. For the interface element displayed in Fig. 4, surrounding nodes are marked by a circle. Absolute displacements and absolute electric potential at the surrounding nodes are expressed in vectors $\boldsymbol{u}^N$ and $\boldsymbol{\Phi}^N$. Corresponding test quantities are denoted as $\boldsymbol{\alpha}^N$ and $\boldsymbol{\beta}^N$. Based on linear interfacial ansatz functions

$$\boldsymbol{N} = [N_{\mathrm{I}}, N_{\mathrm{II}}] = [0.5(1-\xi), 0.5(1+\xi)] \tag{48}$$

referred to interfacial nodes I and II and depending on the interpolation variable $\xi \in [-1, 1]$, discrete jump quantities are expressed as

$$[\![\boldsymbol{\alpha}]\!]^h = \boldsymbol{B} \cdot \boldsymbol{\alpha}^N, \quad [\![\boldsymbol{u}]\!]^h = \boldsymbol{B} \cdot \boldsymbol{u}^N, \quad [\![\beta]\!]^h = \boldsymbol{a} \cdot \boldsymbol{\beta}^N, \quad [\![\varPhi]\!]^h = \boldsymbol{a} \cdot \boldsymbol{\Phi}^N \tag{49}$$

with

$$\boldsymbol{B} = \begin{bmatrix} -N_{\mathrm{I}} & 0 & -N_{\mathrm{II}} & 0 & N_{\mathrm{II}} & 0 & N_{\mathrm{I}} & 0 \\ 0 & -N_{\mathrm{I}} & 0 & -N_{\mathrm{II}} & 0 & N_{\mathrm{II}} & 0 & N_{\mathrm{I}} \end{bmatrix} \tag{50}$$

and

$$\boldsymbol{a} = [-N_{\mathrm{I}}, -N_{\mathrm{II}}, N_{\mathrm{II}}, N_{\mathrm{I}}] \tag{51}$$

whereby $\boldsymbol{B}$ is a nodal operator matrix and $\boldsymbol{a}$ a nodal operator vector. Adopting standard notation, approximated quantities are endowed with an h-index. Following this strategy, the differences of absolute quantities at nodes 4 and 1, and, respectively, 3 and 2 are interpolated over the interface element nodes I and II, compare also Schellekens and De Borst (1993) and Utzinger et al. (2007a).

Applying this discretisation with respect to Eqs. (46) and (47) on the domain of an interface element renders the associated discrete virtual work contributions as

$$G_u^{\mathrm{ie},h} = \int_{\varGamma^{\mathrm{ie}}} \boldsymbol{\alpha}^{N,t} \cdot \boldsymbol{B}^t \cdot \tau([\![\boldsymbol{u}]\!]^h, [\![\varPhi]\!]^h) \mathrm{d}S^{\mathrm{ie}} \tag{52}$$

$$G_\varPhi^{\mathrm{ie},h} = \int_{\varGamma^{\mathrm{ie}}} \boldsymbol{\beta}^{N,t} \cdot \boldsymbol{a}^t \varLambda([\![\boldsymbol{u}]\!]^h, [\![\varPhi]\!]^h) \mathrm{d}S^{\mathrm{ie}} \tag{53}$$

wherein the association with one interface element is indicated by the index ie. Accordingly, residua of an interface element are given as

$$\boldsymbol{f}_u^{\mathrm{ie}} = \int_{\varGamma^{\mathrm{ie}}} \boldsymbol{B}^t \cdot \tau([\![\boldsymbol{u}]\!]^h, [\![\varPhi]\!]^h) \mathrm{d}S^{\mathrm{ie}} \tag{54}$$

$$\boldsymbol{f}_\varPhi^{\mathrm{ie}} = \int_{\varGamma^{\mathrm{ie}}} \boldsymbol{a}^t \varLambda([\![\boldsymbol{u}]\!]^h, [\![\varPhi]\!]^h) \mathrm{d}S^{\mathrm{ie}} \tag{55}$$

to be combined as the interface element residuum vector

$$\boldsymbol{f}^{\mathrm{ie}} = \begin{bmatrix} \boldsymbol{f}_u^{\mathrm{ie}} \\ \boldsymbol{f}_\varPhi^{\mathrm{ie}} \end{bmatrix} \tag{56}$$
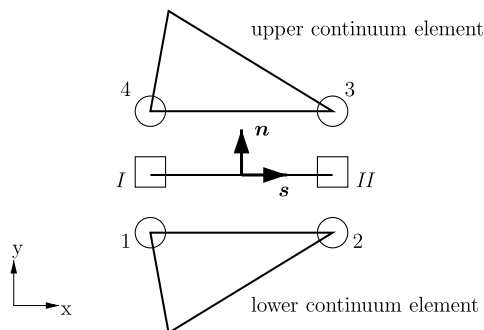

Fig. 4. Schematic sketch of a one-dimensional interface element.

Linearisation of Eqs. (52) and (53) then renders incremental relations on the approximated interface element level, reading as

$$\Delta G_{\boldsymbol{u}}^{\mathrm{ie},h} = \boldsymbol{\alpha}^{N,t} \cdot \underbrace{\left[\int_{\Gamma^{\mathrm{ie}}} \boldsymbol{B}^t \cdot \boldsymbol{C}_{uu}^{\mathrm{alg}} \cdot \boldsymbol{B} \ \mathrm{d}S^{\mathrm{ie}}\right]}_{\boldsymbol{K}_{uu}^{\mathrm{ie}}} \cdot \Delta \boldsymbol{u}^N + \boldsymbol{\alpha}^{N,t} \cdot \underbrace{\left[\int_{\Gamma^{\mathrm{ie}}} \boldsymbol{B}^t \cdot \boldsymbol{c}_{u\Phi}^{\mathrm{alg}} \cdot \boldsymbol{a} \ \mathrm{d}S^{\mathrm{ie}}\right]}_{\boldsymbol{k}_{u\Phi}^{\mathrm{ie}}} \cdot \Delta \boldsymbol{\Phi}^N \tag{57}$$

$$\Delta G_{\Phi}^{\mathrm{ie},h} = \boldsymbol{\beta}^{N,t} \cdot \underbrace{\left[\int_{\Gamma^{\mathrm{ie}}} \boldsymbol{a}^t \cdot \boldsymbol{c}_{\Phi u}^{\mathrm{alg}} \cdot \boldsymbol{B} \ \mathrm{d}S^{\mathrm{ie}}\right]}_{\boldsymbol{k}_{\Phi u}^{\mathrm{ie}}} \cdot \Delta \boldsymbol{u}^N + \boldsymbol{\beta}^{N,t} \cdot \underbrace{\left[\int_{\Gamma^{\mathrm{ie}}} \boldsymbol{a}^t c_{\Phi\Phi}^{\mathrm{alg}} \boldsymbol{a} \ \mathrm{d}S^{\mathrm{ie}}\right]}_{k_{\Phi\Phi}^{\mathrm{ie}}} \cdot \Delta \boldsymbol{\Phi}^N \tag{58}$$

wherein increments of the degrees of freedom are denoted as $\Delta\bullet$, and the underlying algorithmic tangent moduli

$$\boldsymbol{C}_{uu}^{\mathrm{alg}} \quad (2 \times 2), \qquad \boldsymbol{c}_{u\Phi}^{\mathrm{alg}} \quad (2 \times 1), \qquad \boldsymbol{c}_{\Phi u}^{\mathrm{alg}} \quad (1 \times 2), \qquad c_{\Phi\Phi}^{\mathrm{alg}} \quad (1 \times 1) \tag{59}$$

have been introduced, being given in Appendix. Despite the fact that there is no coupling effect for the elastic case, the fatigue damage evolution introduces some coupling due to $\delta = \delta(\llbracket \boldsymbol{u} \rrbracket, \llbracket \Phi \rrbracket)$. Finally, the interface element stiffness matrix follows as

$$\boldsymbol{K}^{\mathrm{ie}} = \begin{bmatrix} \boldsymbol{K}_{uu}^{\mathrm{ie}} & \boldsymbol{k}_{u\Phi}^{\mathrm{ie}} \\ \boldsymbol{k}_{\Phi u}^{\mathrm{ie}} & k_{\Phi\Phi}^{\mathrm{ie}} \end{bmatrix} \tag{60}$$

Please note that, due to the non-associated character of the fatigue law incorporated, the interface element stiffness matrix $\boldsymbol{K}^{\mathrm{ie}}$ turns out to be in general non-symmetric. All interfacial integrals are computed by application of the standard two-point Gauss-integration technique, with $\boldsymbol{f}^{\mathrm{ie}}$ and $\boldsymbol{K}^{\mathrm{ie}}$ to be implemented in a non-linear finite element context.

5. Results and discussion

In the following, different low- and high-cycle-fatigue-motivated boundary conditions are applied to the discretisation shown on the right hand side of Fig. 3, considering mechanical and electrical cycle loading. Both the time-based and the cycle-based model are incorporated, and, consequently, compared. As a starting point, material parameters of the grains, or, respectively, the bulk material, are highlighted in Table 3. All material parameters of the bulk are related to PIC 151. Concerning the material parameters of the interface, no specific stiffness or permittivity values could be retrieved from the literature. Based on Lupascu (2004) and Bast (1985), grain boundaries are supposed to be mechanically weaker than grains, and, moreover, seem to inhere a lower permittivity. The internal length of the interface is a default value and set as $l = 0.3 \times 10^{-6}$ m, related to the width of a grain boundary. Consequently, stiffnesses and permittivities have been academically chosen as

$$c_s = c_n = \frac{[\boldsymbol{C}^\diamond]_{33}^V}{10l}, \quad q = \frac{[\boldsymbol{C}^\diamond]_{33}^V}{l}, \quad \epsilon_r^{\mathrm{init}} = \alpha^{\mathrm{init}} \frac{[\epsilon^\diamond]_{33}}{\epsilon_0 l}, \quad \epsilon_r^{\mathrm{end}} = \alpha^{\mathrm{end}} \frac{[\epsilon^\diamond]_{33}}{\epsilon_0 l} \tag{61}$$

with coupling effects in the interface being neglected. In the examples to be shown, an interfacial permittivity varying with the damage has been assumed, in accordance with Eqs. 26, 28, 29 and $\alpha^{\mathrm{init}} = 1/10$. The material parameters incorporated in the effective quantity δ are chosen as $\beta_s = 1 \ \mathrm{m}^{-1}$, $\beta_n = 1 \ \mathrm{m}^{-1}$, and $\beta_\Phi = 0.01 \ \mathrm{A \ s^3/[kg \ m^2]}$. The comparatively low influence of the electric potential jump is considered to reflect the underlying physical behaviour, as the mechanical and electrical disruption of the grain boundary due to mechanical effects is considered to be dominant. Please note that, to improve numerical accuracy, it is necessary to express the unit of time as $[s] = 10^3$ ms for all computational input parameters.

5.1. Time-based fatigue computations

For the examples of this section, the time-based material law is applied, see Section 3.1. The FE-discretisation introduced in the above serves as input for a non-linear FE-program, together with appropriate boundary conditions. The material parameter has been chosen as $\alpha = 4 \times 10^{-7}$.

Table 3
Material parameters in the bulk

$\lambda = 0.0630 \times 10^{12} \ (\mathrm{N/m^2})$
$\mu_\perp = 0.0222 \times 10^{12} \ \mathrm{N/m^2}$
$\mu_\parallel = 0.0196 \times 10^{12} \ \mathrm{N/m^2}$
$\zeta = 0.0007 \times 10^{12} \ \mathrm{N/m^2}$
$\eta = 0.0018 \times 10^{12} \ \mathrm{N/m^2}$
$[\boldsymbol{e}^\diamond]_{31}^V = 0.0397 \times 10^2 \ \mathrm{A \ s/m^2}$
$[\boldsymbol{e}^\diamond]_{33}^V = 0.2879 \times 10^2 \ \mathrm{A \ s/m^2}$
$[\boldsymbol{e}^\diamond]_{15}^V = 0.1197 \times 10^2 \ \mathrm{A \ s/m^2}$
$[\epsilon^\diamond]_{11} = 17152 \times 10^{-12} \ \mathrm{A^2 \ s^4/[kg \ m^3]}$
$[\epsilon^\diamond]_{33} = 18685 \times 10^{-12} \ \mathrm{A^2 \ s^4/[kg \ m^3]}$

5.1.1. Displacement loading

The boundary conditions of the first example are schematically shown in Fig. 5. On the right hand side, it is shown that on the upper boundary of the rectangular model, cyclic displacements are applied. On the left hand side of Fig. 5, the same cyclic
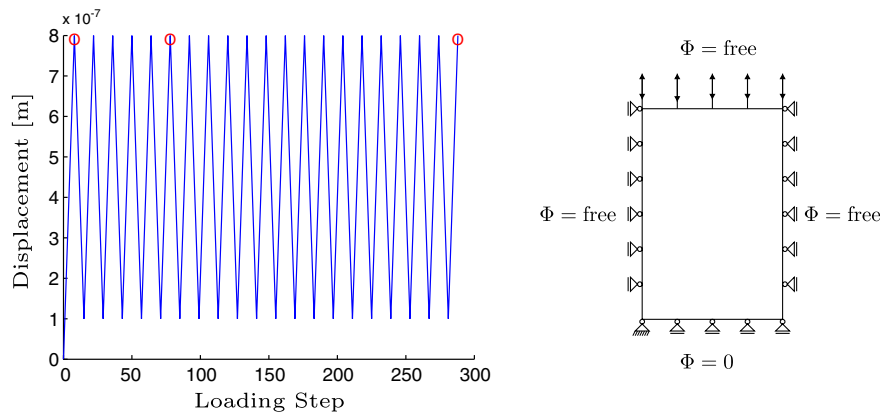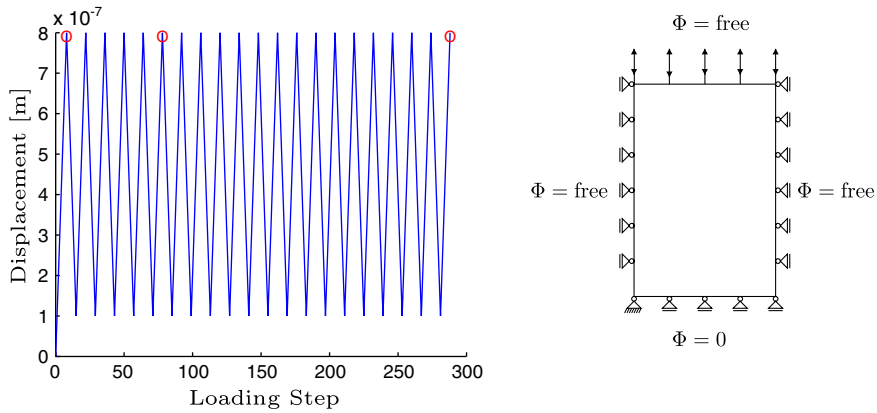

**Fig. 5.** Loading history (left) and boundary conditions (right, cyclic displacements): increasing interfacial permittivity. (For interpretation of the references to colour in the citation of this figure, the reader is referred to the web version of the article.)
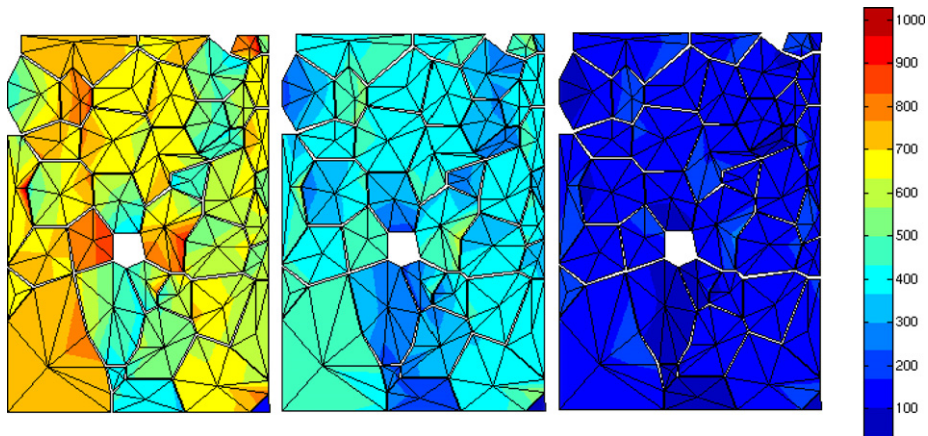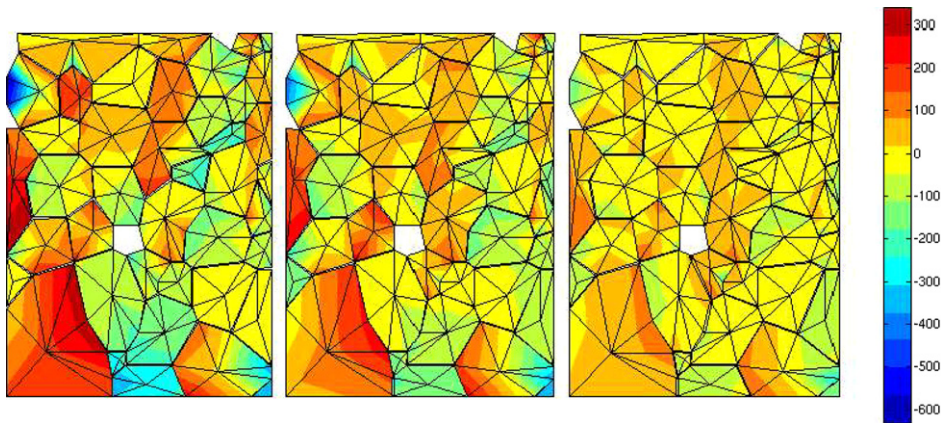

Fig. 6. σ_{yy} [MPa] after 0 (left), 5 (middle), and 20 (right) cycles.
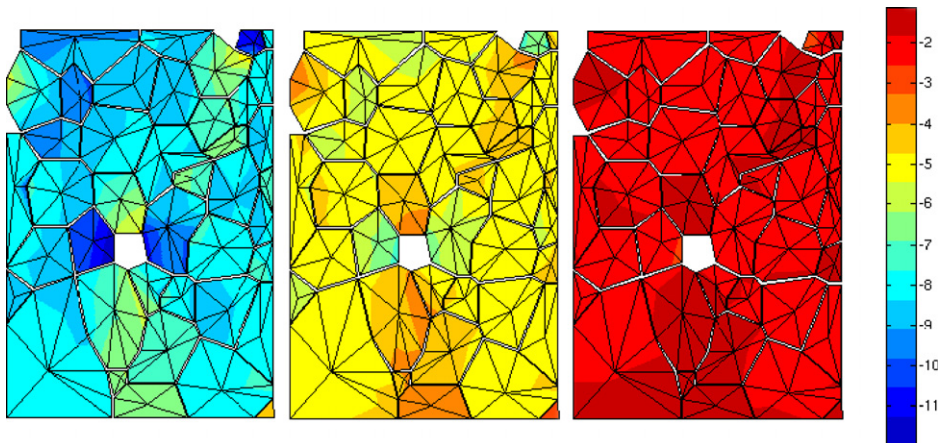
Fig. 7. E_y [MV/m] after zero (left), 5 (middle), and 20 (right) cycles.

displacements are plotted over the number of loading steps. The cyclic load is applied such that it is always in the global range of tensile loading, with 14 loading steps for each cycle, and 288 steps in total to simulate 20 cycles including one additional loading step for the first loading sequence. The resulting stresses in vertical direction in the bulk, denoted as σ_{yy}, are
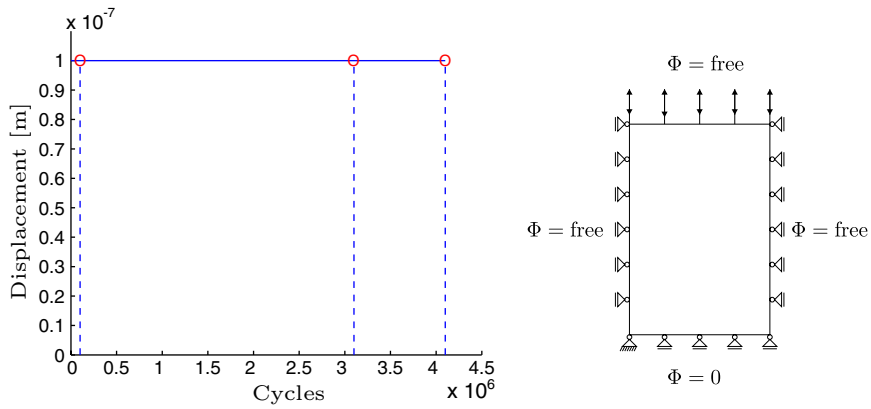

Fig. 8. Loading history (left) and boundary conditions (right, cyclic displacements): decreasing interfacial permittivity.
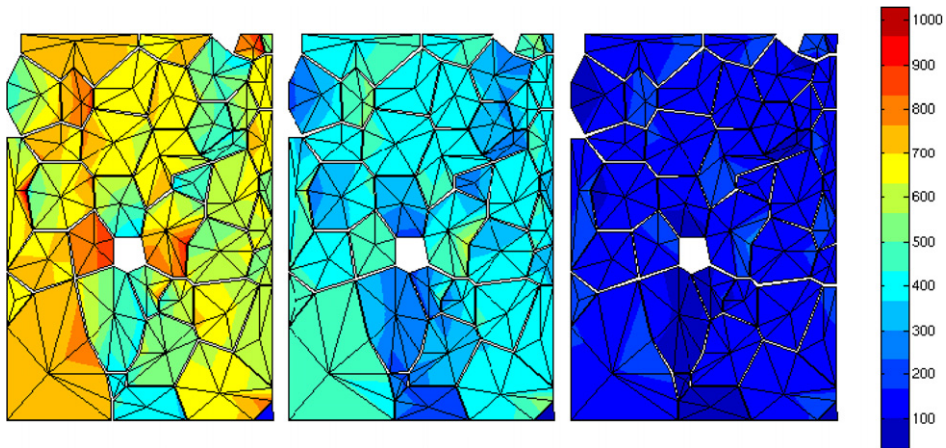

Fig. 9. σ_{yy} [MPa] after 0 (left), 5 (middle), and 20 (right) cycles.
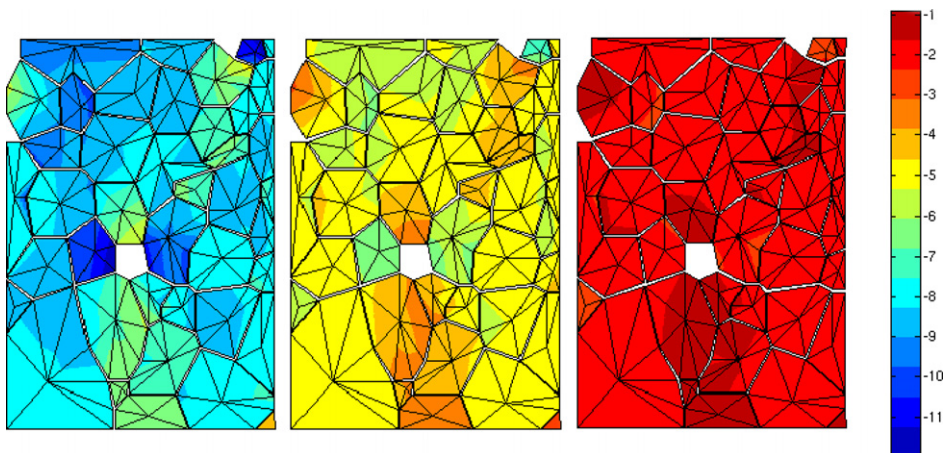
Fig. 10. E_y [MV/m] after 0 (left), 5 (middle), and 20 (right) cycles.

displayed in Fig. 6, while the electric field in vertical direction in the bulk, E_y, is shown in Fig. 7. In both figures, snapshots are taken after the first loading amplitude ($\doteq 0$ cycles), 5 and 20 cycles, all of them being marked in Fig. 5 by red circles. Fig. 6 shows that the stresses σ_{yy} decrease under continued cycling. This clearly accompanies a damage-related stiffness decrease. With a damage-induced increasing permittivity in mind ($\alpha^{\text{end}} = 3/10$), and only considering electric effects, the electric po-
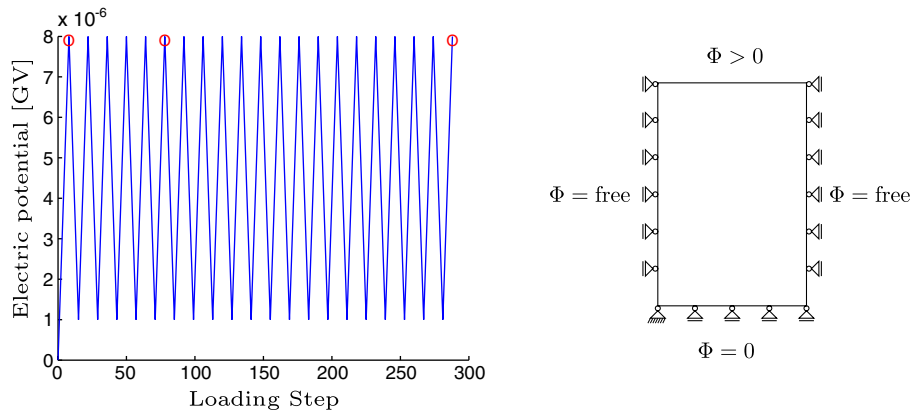
Fig. 11. Loading history (left) and boundary conditions (right, cyclic electric potential): increasing interfacial permittivity.

Fig. 12. σ_{yy} [MPa] after 0 (left), 5 (middle), and 20 (right) cycles.
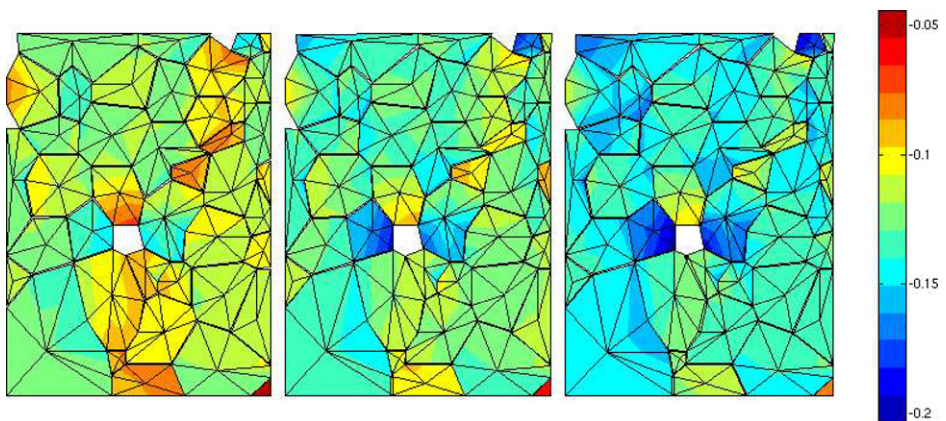
Fig. 13. E_y [GV/m] after 0 (left), 5 (middle), and 20 (right) cycles.

tential jump over the interface would tend to decrease, and, in consequence, a related fraction of the electric field in the bulk would increase to compensate this. Hence, the fraction of strains in the bulk related to this is raised by some amount. In turn, this raises the displacement jumps in the interface, supporting damage evolution. For the current $\beta_\Phi \ll \beta_s = \beta_n$, mostly the

Fig. 14. Loading history (left) and boundary conditions (right, cyclic displacements): increasing interfacial permittivity.
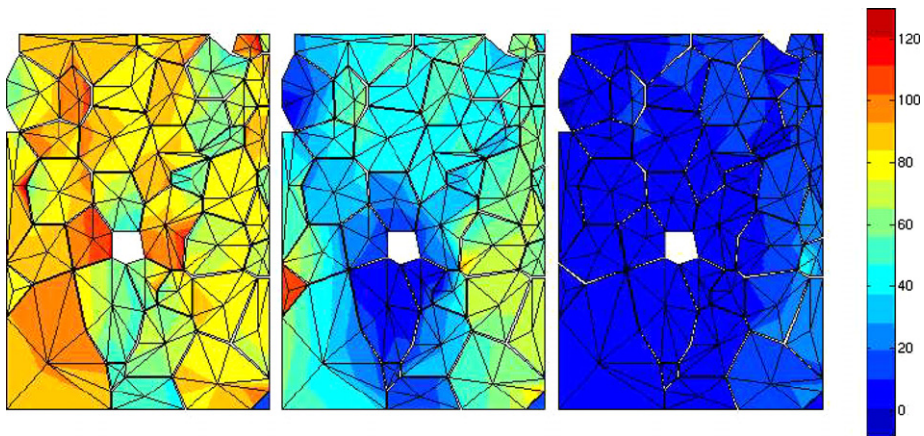
Fig. 15. σ_{yy} [MPa] after 10^5 (left), 3.1×10^6 (middle), and 4.1×10^6 (right) cycles.
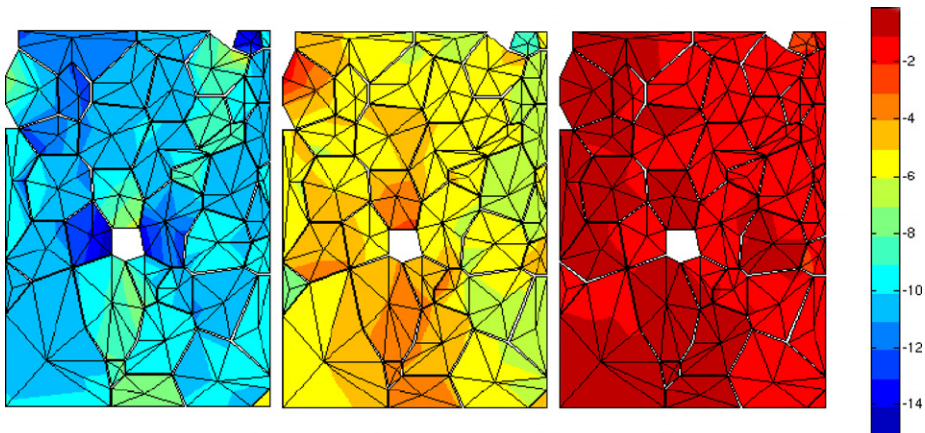
Fig. 16. E_y [10^2 kV/m] after 10^5 (left), 3.1×10^6 (middle), and 4.1×10^6 (right) cycles.

displacement jump contributes to the damage. Considering the overall constitutive answer, the decreasing absolute value of the electric field component E_y, as shown in Fig. 7, seems to be due to the dominant influence of decreasing interfacial stiffnesses. For a lower stiffness in the interface, strains in the bulk decrease, and, simultaneously, also a large reduction of the
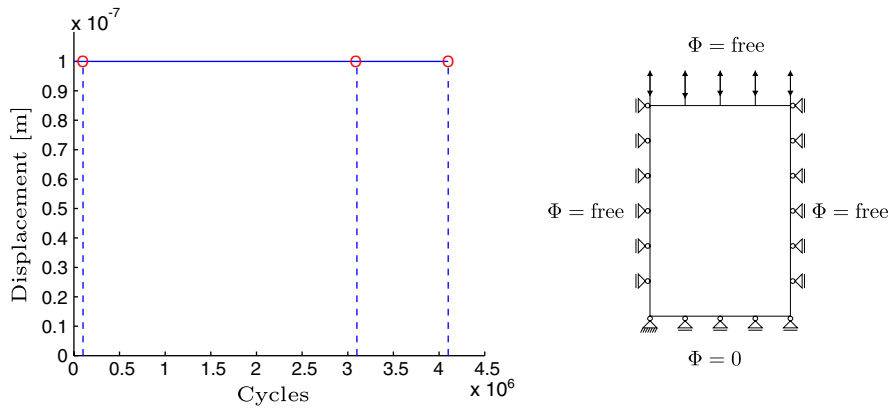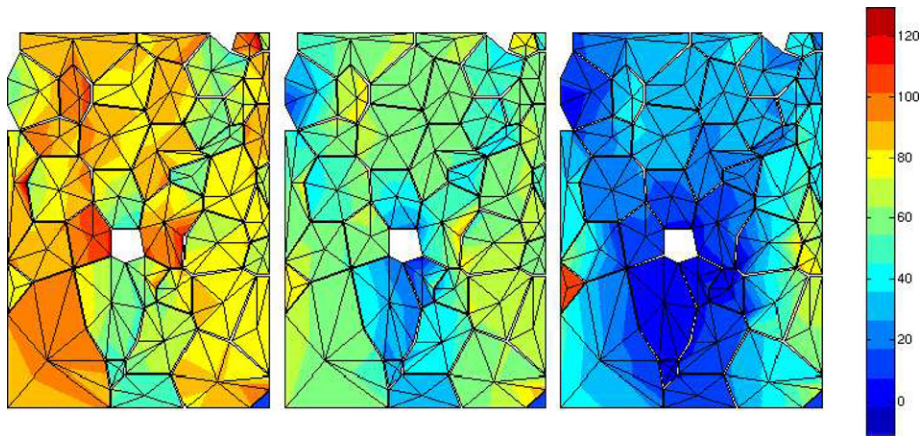

Fig. 17. Loading history (left) and boundary conditions (right, cyclic displacements): decreasing interfacial permittivity.

Fig. 18. σ_{yy} [MPa] after 10^5 (left), 3.1×10^6 (middle), and 4.1×10^6 (right) cycles.
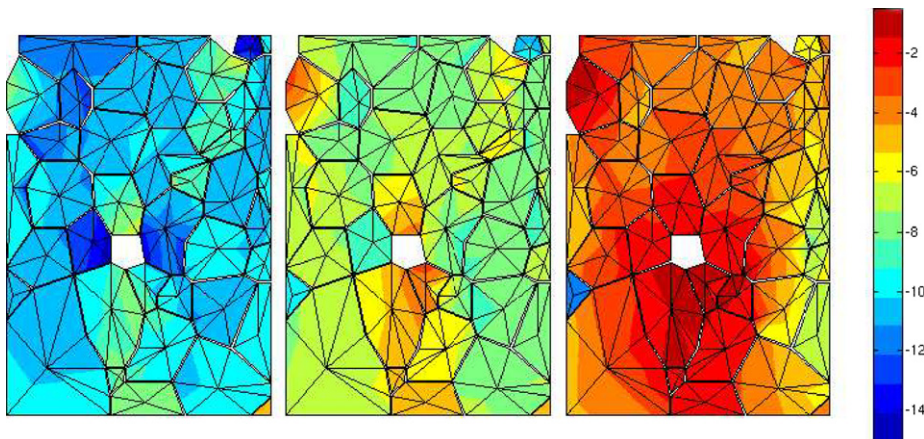
Fig. 19. E_y [10^2 kV/m] after 10^5 (left), 3.1×10^6 (middle), and 4.1×10^6 (right) cycles.

absolute value of the electric field E_y will occur. The prevailing role of stiffnesses seem to be induced by the mechanical boundary conditions of cyclic displacement loading, while, simultaneously, at the upper boundary of the specimen, the electric potential boundary condition is free. Therefore, the electrical field behaviour in the bulk is dominated by the mechanical response, leading to decreasing values of E_y due to decreasing stiffnesses.
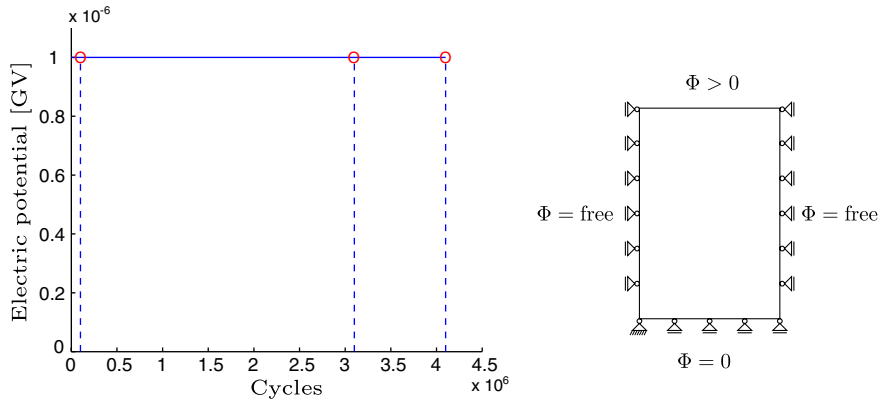

Fig. 20. Loading history (left) and boundary conditions (right, cyclic electric potential): increasing interfacial permittivity.
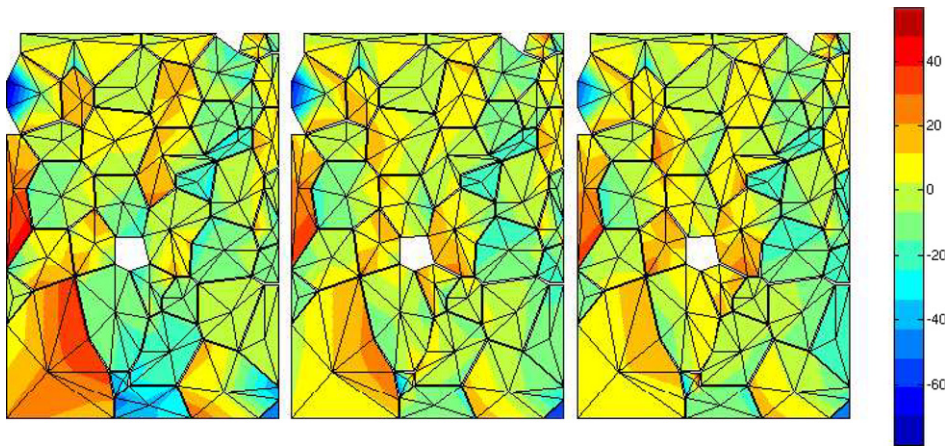

Fig. 21. σ_{yy} [MPa] after 10^5 (left), 3.1×10^6 (middle), and 4.1×10^6 (right) cycles.
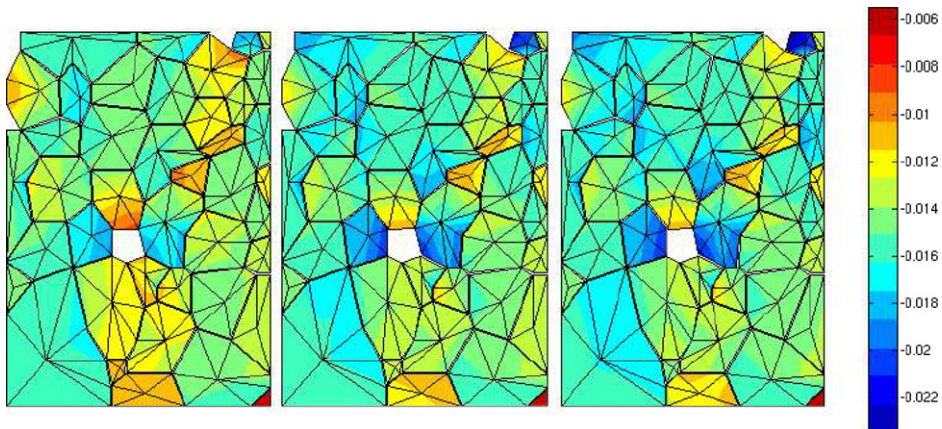

Fig. 22. E_y [GV/m] after 10^5 (left), 3.1×10^6 (middle), and 4.1×10^6 (right) cycles.

For similar boundary conditions (see Fig. 8) and a decreasing permittivity ($\alpha^{\text{end}} = 1/100$), the electric potential jump would tend to increase. Consequently, this effect does not assist the bulk strains to increase, and therefore, in the sense of the correlations described in the above, this effect does not support the damage evolution. With Fig. 9 revealing solely a slight influence of this effect for the stresses σ_{yy}, the electric field E_y given in Fig. 10 shows a smaller decrease as compared to Fig. 7.

5.1.2. Electric potential loading

In contrast, for a cyclic electric potential, adequate boundary conditions are found in Fig. 11. Again, seven loading steps are chosen for loading and unloading within one cycle, resulting in 288 loading steps for 20 cycles, including one more loading step in the first loading sequence. Moreover, Figs. 12 and 13 display snapshots after the first loading amplitude ($\doteq 0$ cycles), 5 and 20 cycles. The interfacial permittivity is considered to increase, i.e. $\alpha^{\text{end}} = 3/10$. Concerning the electric field component in vertical direction, E_y, Fig. 13 shows that the absolute value of E_y increases with continued cycling. This can be related to increasing permittivities in the interfaces. With a cyclic electric potential given as a boundary condition, no displacements are prescribed for the upper boundary. Therefore, it is considered that electric fatigue effects superpose mechanical-related effects concerning the absolute value of the electric field component E_y. This is not the case for the stresses σ_{yy}, displayed in Fig. 12. There, mechanical influences still prevail and stresses are reduced with continued cycling.

5.2. Cycle-based fatigue computations

Concerning cycle-based fatigue, the boundary conditions are essentially similar to the boundary conditions of Sections 5.1.1 and 5.1.2, with a difference referred to the number of cycles and the numerical implementation. The appropriate material law is discussed in Section 3.2. Material parameters have been chosen as $C = 1.5 \times 10^9$, $\beta = 1$, and $\gamma = 0$.

5.2.1. Displacement loading

For the case of cyclic displacement loading, boundary conditions are given in Fig. 14. In view of the numerical implementation, displacements are applied in the first loading step. In subsequent loading steps, the displacements, given at the upper boundary, are fixed. For each loading step, $\Delta N = 10^5$ cycles are assumed to take place, resulting in 4.1×10^6 cycles distributed on 41 loading steps. This is illustrated on the left hand side of Fig. 14. Snapshots are taken after 10^5, 3.1×10^6, and 4.1×10^6 cycles. At first, increasing interfacial permittivities are assumed ($\alpha^{\text{end}} = 3/10$). Stresses in vertical direction σ_{yy} are given in Fig. 15 while the electric field component in vertical direction E_y is displayed in Fig. 16. As Fig. 15 reveals, stresses σ_{yy} decrease due to decreasing stiffnesses induced by cycle-based fatigue. Simultaneously, the absolute values of the vertical electric field component E_y also decrease. This seems to be due to the superposition of electric effects by mechanical effects as described in Section 5.1.1, caused by dominant mechanical boundary conditions.

For identical boundary conditions (Fig. 17) and a decreasing permittivity with $\alpha^{\text{end}} = 1/100$, the damage evolution is less pronounced for reasons as described in Section 5.1.1. This is understood by comparing the stresses σ_{yy} of Figs. 15 and 18 and the electric field component E_y of Figs. 16 and 19. As observed from Figs. 18 and 19, this effect is for the cycle-based fatigue even more significant as for the time-based fatigue of Section 5.1.1.

5.2.2. Electric potential loading

In view of electric potential loading, boundary conditions are illustrated in Fig. 20. Again, each loading step represents $\Delta N = 10^5$ cycles as explained in Section 5.2.1. In this context, snapshots are once more taken after 10^5, 3.1×10^6, and 4.1×10^6 cycles. Interfacial permittivities are considered to increase, i.e. $\alpha^{\text{end}} = 3/10$. The corresponding plots of the stresses in vertical direction σ_{yy} are given in Fig. 21, while the vertical component of the electric field E_y is displayed in Fig. 22, revealing increasing absolute values of E_y corresponding to increasing interfacial permittivities. According to the precedent examples, electrical effects seem to match the intensity of mechanical effects concerning the absolute value of the electric field component E_y. Moreover, it emerges that concerning the stresses σ_{yy}, mechanical influences still prevail and stresses are reduced with continued cycling.

5.3. Discussion

Subsequently, some important aspects concerning the above results are discussed.

5.3.1. Comparison of the time-based and cycle-based fatigue evolution

First of all, it is noteworthy that for the two fatigue-damage evolutions described in Sections 3.1 and 3.2, different functional dependencies are incorporated. This must clearly result in different types of the damage evolution. In Fig. 23, the damage parameter is plotted over the number of load steps for the time-based fatigue example of Sections 5.1.1 and 5.1.2 for increasing permittivities. The damage parameter d is displayed for the Gauss point marked in Fig. 3. The step patterns result from the fact that only for loading, the damage parameter is updated. Moreover, it is recognised that the damage evolution for cyclic electric potential loading is more progressive than for cyclic displacement loading. Similar dependencies for cycle-based fatigue are shown in Fig. 24. Please note that, for the Gauss point considered, the damage cut-off is reached after 30×10^5 cycles for displacement loading. However, different evolution techniques for time-based and cycle-based fatigue
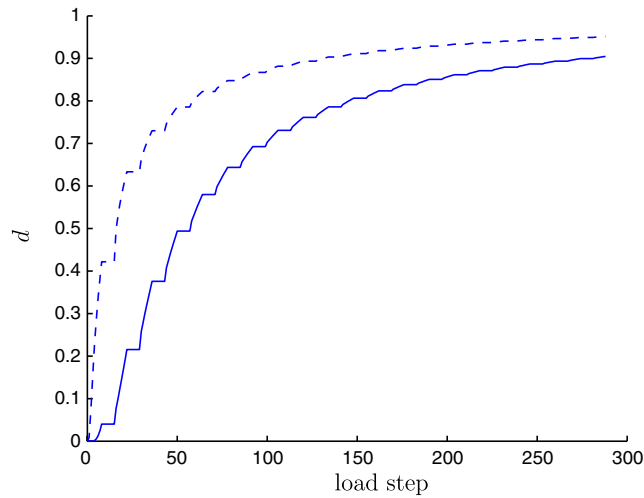
Fig. 23. Time-based fatigue: damage parameter *d* over number of load steps. Solid line: displacement loading, dotted line: electric potential loading.
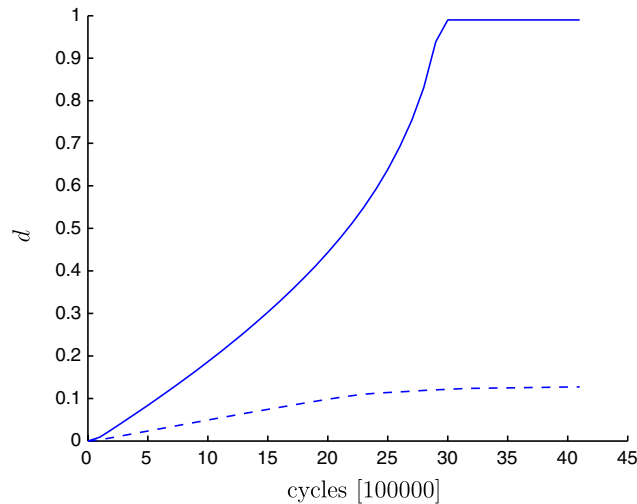

Fig. 24. Cycle-based fatigue: damage parameter *d* over number of cycles. Solid line: displacement loading, dotted line: electric potential loading.

damage lead to different evolutions concerning, e.g., stresses or the electric field components. Furthermore, the cycle-based fatigue evolutions seem to provide more freedom to be fitted to experimental data due to a larger number of material parameters. In this context, only academic simulations are accomplished, and comparisons with experiments would give further information on the practicability of the models. Indeed, before considering comparisons with measurements, further significant attributes of piezoelectric material behaviour, for example switching effects, should additionally be included in the computational formulation.

5.3.2. On neglected coupling effects in the interface and the role of β_s, β_n, and β_Φ

With the numerical examples discussed above, interfacial coupling effects have been neglected in order to model the very reduced coupling abilities occurring along the amorphous grain boundaries. Direct consequences thereof are as follows: if cyclic displacement boundary conditions are applied to an interface, and, at the same time, electric potential boundary conditions at the top of the specimen are free, mostly the interfacial displacement jumps are cycled, whereas the electric potential jumps are affected in a smaller amount, not being coupled to the displacement jumps. From this it can be concluded that displacement jumps and stiffnesses in the interface will dominate the stresses and the electric field in the bulk, triggered by interfacial effects. The interfacial electric potential jumps are then influenced by the damage variable and the related change of permittivity, and, as inherent to the overall solution of the coupled BVP, the bulk itself. Here, however, the electric potential jump influences the bulk only in a small amount. Moreover, mainly displacement jumps would contribute to the damage

evolution. Analogous effects occur when the mechanical boundary conditions at the top of the specimen are free and a cyclic electric potential is applied. Then, mainly electric potential jumps would contribute to the damage evolution and bulk actions are dominated by interfacial electric potential jumps and permittivities. Nevertheless, no matter which degrees of freedom are cycled, the associated damage variable will always be applied to both the interfacial stiffnesses and permittivities. What clearly influences the weight of displacement or electric potential jumps concerning damage evolution are the damage material parameters β_s, β_n, and β_Φ, see also Eq. (31). In the current work, β_Φ has been chosen much smaller than β_s, β_n which is considered to reflect some physics of piezoceramic grain boundaries. Consequently, the role of the electric potential jump and of varying permittivities is reduced as compared to the influence of the displacement jump and reduced stiffnesses.

These correlations are generally reflected by the simulation results. For cyclic displacements combined with the time-based or the cycle-based fatigue model, stresses σ_{yy} are decreasing due to decreasing stiffnesses. Simultaneously, the absolute value of the electric field component E_y is also decreasing due to the dominant role of interfacial displacement jumps – the electric potential at the upper boundary is free. For cyclic electric potentials and both fatigue models, the absolute values of the electric field components E_y rise with continued cycling, which can be correlated to the dominant role of the interfacial electric potential jumps and the related increase of permittivities which has been assumed in those examples. In view of the stresses σ_{yy}, mechanical influences still prevail, and a decrease is observed, due to the small value of β_Φ and the electric-field-induced increase of the bulk strains, promoting increasing interfacial displacement jumps.

5.3.3. Influence of increasing and decreasing interfacial permittivities

For both the time-based and the cycle-based fatigue computations, increasing and decreasing interfacial permittivities have been investigated for cyclic displacement boundary conditions. Concerning the overall constitutive behaviour, the cyclic displacement boundary conditions induce that the overall electric field is triggered by the strains, both decreasing with increasing damage with respect to the cycling history. The damage is directly influenced by the interfacial jump quantities. Due to the small weighting factor β_Φ, the direct influence of the potential jump and the permittivities is of minor significance; nevertheless, they still indirectly influence the overall damage, though being strongly superposed by mechanical effects.

For increasing permittivities, the electric potential jump over the interface would tend to decrease. Hence, a related fraction of the electric field in the bulk would increase to compensate this and the related fraction of bulk strains would then be raised by some amount due to piezoelectric coupling. As a consequence, this raises the displacement jumps in the interface, which supports the damage evolution. Contrariwise, for decreasing permittivities, the electric potential jump over the interface would tend to increase, causing a certain fraction of the bulk strains to decrease. Such behaviour would decrease the displacement jumps in the interface, restraining the damage evolution to some amount. Consequently, such effects are indicated in the results. Due to the circumstances discussed in the above, for decreasing permittivities, stresses σ_{yy} and the electric field component E_y decrease less than for increasing permittivities, which stems from some restrained damage evolution.

5.3.4. Influences of grain structure and discretisation

For the micrograph considered, compare Fig. 3, a void is present in the middle of the discretisation. For cyclic displacements and both fatigue models, but especially for the cycle-based fatigue evolution, fatigue-motivated damage starts in an area around the mentioned void, compare Figs. 15, 16, 18 and 19.

Concerning the discretisation of the continuum, linear triangular elements have been applied, inhering rather poor approximation abilities compared to the application of higher order ansatz functions or finer meshes. Nevertheless, the discretisation used turns out to reflect all important properties of the academic example investigated.

6. Conclusions

A SEM-obtained mesostructure (Nuffer et al. (2000)) of the piezoelectric material PIC 151 has been discretised by applying linear triangular finite elements for the grains and linear interface elements for the grain boundaries. Different fatigue-loading-motivated boundary conditions have been applied to the discretisation. In this context, a first attempt has been made to model such a structure, emphasising the grain boundary behaviour. For the grains, or rather the bulk material, a linear and coupled material law has been implemented. Concerning the grain boundaries, discretised by interface or, respectively, cohesive-type elements, two different material models have been considered: the first appropriate by capturing low-cycle-fatigue, and the second material model being able to reflect high-cycle-fatigue behaviour. For the bulk, PIC 151-like material parameters have been incorporated. In view of the interface, an effective parameter δ has been incorporated into the fatigue-motivated damage evolution, being academic in nature due to missing reliable information on the exact physical processes in grain boundaries under fatigue loading. Electrical and mechanical effects have been decoupled concerning the linear response. The first interfacial material model, reflecting low-cycle-fatigue behaviour, is of an exponential format. It is entitled "time-based fatigue formulation" and explicitly tracks the loading history of single cycles. In contrast, a second interfacial material model, also being of an exponential though of different format, captures high-cycle-fatigue behaviour by directly incorporating a certain number of cycles. It has been entitled as "cycle-based fatigue formulation". The related damage parameter d is constrained by the driving force in a thermodynamical consistent framework. For the chosen academic examples it turned out that the proposed assumptions of a fatigue-related decrease of interfacial mechanical tractions

and varying permittivities are reflected in the results. So far, the literature does not clearly reveal experimental results concerning the permittivity behaviour under fatigue-related loading boundary conditions. Anyhow, literature reveals that grain boundary permittivity is generally lower than the permittivity of the grains.

In view of the fact that only permittivities and stiffnesses are accounted for in this work, it is clear that realistic grain boundaries must inhere further and more complex phenomena under fatigue loading than those incorporated here. In this context, it is necessary to prospect for new experimental results and to improve knowledge concerning the fatigue-related grain boundary behaviour. As this is just a first step towards an integral modelling of a fatigued piezoelectric mesostructure, non-linear effects as phase transformations have to be included in the bulk constitutive response in the future. To model polarisation switching of domain structures, e.g., internal variable methods can be applied (e.g., Lynch and McMeeking (1994), Lynch (1998), Arockiarajan et al. (2006), Arockiarajan and Menzel (2007), Menzel et al. (2008)).

Furthermore, it is a matter of ongoing research to include cohesive laws possibly substantially different to the ones presented in this work. In this regard, a capacitor-like behaviour of the interface is investigated. Additionally, fracture energy related models are considered. Another field of interest constitutes the bifurcation analysis of the related continuum-interface problem, see, e.g., Utzinger et al., 2007b for a discussion on a related non-coupled problem. Finally, when the mesomechanical material models are accurate enough, an incorporation into multiscale computations is considered.

Acknowledgements

Appendix A. Algorithmic tangent moduli

In the following, the algorithmic tangents appearing in Section 4.3 are given for the cases of fatigue evolution.

A.1. Time-based fatigue formulation

$$\boldsymbol{C}_{uu}^{\text{alg}} = [1 - d_{n+1}]\boldsymbol{C} - \exp\left(-\frac{\alpha}{\tilde{\delta}_{n+1}}\right)\alpha\tilde{\delta}_{n+1}^{-2}\delta_{n+1}^{-1}[\boldsymbol{C}\cdot[\![\boldsymbol{u}]\!]_{n+1}]\otimes\sum_i\beta_i^2[\![\boldsymbol{u}_i]\!]_{n+1} \tag{A.1}$$

$$\boldsymbol{c}_{u\Phi}^{\text{alg}} = -\exp\left(-\frac{\alpha}{\tilde{\delta}_{n+1}}\right)\alpha\tilde{\delta}_{n+1}^{-2}\delta_{n+1}^{-1}\beta_\Phi^2[\![\Phi]\!]_{n+1}[\boldsymbol{C}\cdot[\![\boldsymbol{u}]\!]_{n+1}] \tag{A.2}$$

$$\boldsymbol{c}_{\Phi u}^{\text{alg}} = -\epsilon_0[\epsilon_r^{\text{end}} - \epsilon_r^{\text{init}}][\![\Phi]\!]_{n+1}\exp\left(-\frac{\alpha}{\tilde{\delta}_{n+1}}\right)\alpha\tilde{\delta}_{n+1}^{-2}\delta_{n+1}^{-1}\sum_i\beta_i^2[\![\boldsymbol{u}_i]\!]_{n+1} \tag{A.3}$$

$$c_{\Phi\Phi}^{\text{alg}} = -\epsilon_0\epsilon_r(d_{n+1}) - \epsilon_0[\epsilon_r^{\text{end}} - \epsilon_r^{\text{init}}][\![\Phi]\!]_{n+1}\exp\left(-\frac{\alpha}{\tilde{\delta}_{n+1}}\right)\alpha\tilde{\delta}_{n+1}^{-2}\delta_{n+1}^{-1}\beta_\Phi^2[\![\Phi]\!]_{n+1} \tag{A.4}$$

A.2. Cycle-based fatigue formulation

$$\boldsymbol{C}_{uu}^{\text{alg}} = [1 - d_{N+\Delta N}]\boldsymbol{C} - \frac{1}{2}\Delta N\,C\exp(\gamma d_{\text{p}})\delta_{a,N+\Delta N}^{\beta-1}[\boldsymbol{C}\cdot[\![\boldsymbol{u}]\!]_{N+\Delta N}]\otimes\sum_i\beta_i^2[\![\boldsymbol{u}_i]\!]_{N+\Delta N} \tag{A.5}$$

$$\boldsymbol{c}_{u\Phi}^{\text{alg}} = -\frac{1}{2}\Delta N\,C\exp(\gamma d_{\text{p}})\delta_{a,N+\Delta N}^{\beta-1}\beta_\Phi^2[\![\Phi]\!]_{N+\Delta N}[\boldsymbol{C}\cdot[\![\boldsymbol{u}]\!]_{N+\Delta N}] \tag{A.6}$$

$$\boldsymbol{c}_{\Phi u}^{\text{alg}} = -\epsilon_0[\epsilon_r^{\text{end}} - \epsilon_r^{\text{init}}][\![\Phi]\!]_{N+\Delta N}\frac{1}{2}\Delta N\,C\exp(\gamma d_{\text{p}})\delta_{a,N+\Delta N}^{\beta-1}\sum_i\beta_i^2[\![\boldsymbol{u}_i]\!]_{N+\Delta N} \tag{A.7}$$

$$c_{\Phi\Phi}^{\text{alg}} = -\epsilon_0\epsilon_r(d_{N+\Delta N}) - \epsilon_0[\epsilon_r^{\text{end}} - \epsilon_r^{\text{init}}][\![\Phi]\!]_{N+\Delta N}\frac{1}{2}\Delta N\,C\exp(\gamma d_{\text{p}})\delta_{a,N+\Delta N}^{\beta-1}\beta_\Phi^2[\![\Phi]\!]_{N+\Delta N} \tag{A.8}$$

References

Arias, I., Serebrinsky, S., Ortiz, M., 2006. A phenomenological cohesive model of ferroelectric fatigue. Acta Mater. 54, 975–985.

Arockiarajan, A., Menzel, A., 2007. On the modelling of rate-dependent domain switching in piezoelectric materials under superimposed stresses. Comput. Model. Eng. Sci. 19 (2), 163–180, printed version: 20 (1), 55–72.

Arockiarajan, A., Menzel, A., Delibas, B., Seemann, W., 2006. Computational modelling of rate-dependent domain switching in piezoelectric materials. Eur. J. Mech. A Solids 25, 950–964.

Bast, U., 1985. Eigenschaften der Sekundärphase $Ba_6Ti_{17}O_{40}$ und ihr Einfluss auf $BaTiO_3$-Keramik. Ph.D. thesis, Universität Erlangen-Nürnberg.

Cirak, F., Ortiz, M., Pandolfi, A., 2005. A cohesive approach to thin-shell fracture and fragmentation. Comput. Meth. Appl. Mech. Eng. 194, 2604–2618.

Corigliano, A., Mariani, S., Pandolfi, A., 2006. Numerical analysis of rate-dependent dynamic composite delamination. Compos. Struct. 66, 766–775.

Daining, F., Liu, D., Sun, C., 2004. Fatigue crack growth in ferroelectric ceramics driven by alternating electric fields. J. Am. Ceram. Soc. 87, 840–846.

Ekh, M., Menzel, A., Runesson, K., Steinmann, P., 2003. Anisotropic damage with the MCR effect coupled to plasticity. Int. J. Eng. Sci. 41, 1535–1551.

Erinc, M., Schreurs, P., Geers, M., 2007. Integrated numerical-experimental analysis of interfacial fatigue fracture in SnAgCu solder joints. Int. J. Solids Struct. 44, 5680–5694.

Eringen, A.C., Maugin, G.A., 1989. Electrodynamics of continua. I. Foundations and Solid Media. Springer.

Espinosa, H., Zavattieri, P., 1999. Modeling of ceramic microstructures: dynamic damage initiation and evolution. Shock Compress. Conden. Matter, 333–338.

Jansson, N., Larsson, R., 2001. A damage model for simulation of mixed-mode delamination growth. Compos. Struct. 53, 409–417.

Kamlah, M., 2001. Ferroelectric and ferroelastic piezoceramics – modeling of electromechanical hysteresis phenomena. Contin. Mech. Thermodyn. 13, 219–268.

Kamlah, M., Böhle, U., 2001. Finite element analysis of piezoceramic components taking into account ferroelectric hysteresis behaviour. Int. J. Solids Struct. 38, 605–633.

Klinkel, S., 2006a. A phenomenological constitutive model for ferroelastic and ferroelectric hysteresis effects in ferroelectric ceramics. Int. J. Solids Struct. 43, 7197–7222.

Klinkel, S., 2006b. A thermodynamic consistent 1d model for ferroelastic and ferroelectric hysteresis effects in piezoceramics. Commun. Numer. Meth. Eng. 22, 727–739.

Knauer, U., 1982. Submikronanalyse von $BaTiO_3$-Keramik im Elektronenmikroskop zum Studium von Gefügeausbildung und elektrischen Eigenschaften. Ph.D. thesis, Universität Erlangen-Nürnberg.

Larsson, R., Jansson, N., 2002. Geometrically non-linear damage interface based on regularized strong discontinuity. Int. J. Numer. Meth. Eng. 54, 473–497.

Lemaitre, J., 1994. A Course on Damage Mechanics. Springer.

Lemaitre, J., Chaboche, J.-L., 1994. Mechanics of Solid Materials. Cambridge University Press.

Lohkämper, R., Neumann, H., Arlt, G., 1990. Internal bias in acceptor-doped $BaTiO_3$ ceramics: numerical evaluation of increase and decrease. J. Appl. Phys. 68, 4220–4224.

Lupascu, D.C., 2004. Fatigue in Ferroelectric Ceramics and Related Issues. Springer.

Lynch, C., 1998. On the development of multiaxial phenomenological constitutive laws for ferroelectric ceramics. J. Intell. Mater. Syst. Struct. 9, 555–563.

Lynch, C., McMeeking, R., 1994. Finite strain ferroelectric constitutive laws. Ferroelectrics 160, 177–184.

Maugin, G.A., 1988. Continuum Mechanics of Electromagnetic Solids, North-Holland.

Mehling, V., Tsakmakis, C., Gross, D., 2007. Phenomenological model for the macroscopical material behavior of ferroelectric ceramics. J. Mech. Phys. Solids 55, 2106–2141.

Menzel, A., Arockiarajan, A., Sivakumar, S., 2008. Two models to simulate rate-dependent domain switching effects – application to ferroelastic polycrystalline ceramics. Smart Mater. Struct. 17, 015026 (13pp).

Menzel, A., Steinmann, P., 2001. A theoretical and computational setting for anisotropic continuum damage mechanics at large strains. Int. J. Solids Struct. 38 (52), 9505–9523.

Munoz, J., Galvanetto, U., Robinson, P., 2006. On the numerical simulation of fatigue driven delamination with interface elements. Int. J. Fatig. 28, 1136–1146.

Nguyen, O., Repetto, E., Ortiz, M., Radovitzky, R., 2001. A cohesive model of fatigue crack growth. Int. J. Frac. 110, 351–369.

Nuffer, J., Lupascu, D., Rödel, J., 2000. Damage evolution in ferroelectric PZT-induced by bipolar electric cycling. Acta Mater. 48, 3783–3794.

Ortiz, M., Pandolfi, A., 1999. Finite-deformation irreversible cohesive elements for three-dimensional crack-propagation analysis. Int. J. Numer. Meth. Eng. 44, 1267–1282.

Paas, M., Schreurs, P., Brekelmans, W., 1993. A continuum approach to brittle and fatigue damage: theory and numerical procedures. Int. J. Solids Struct. 30, 579–599.

Pandolfi, A., Krysl, P., Ortiz, M., 1999. Finite element simulation of ring expansion and fragmentation: the capturing of length and time scales through cohesive models of fracture. Int. J. Frac. 95, 279–297.

Pandolfi, A., Ortiz, M., 1998. Solid modeling aspects of three-dimensional fragmentation. Eng. Comput. 14, 287–308.

Peerlings, R., Brekelmans, W., de Borst, R., Geers, M., 2000. Gradient-enhanced damage modelling of high-cycle fatigue. Int. J. Numer. Meth. Eng. 49, 1547–1569.

Robinson, P., Galvanetto, U., Tumino, D., Bellucci, G., Violeau, D., 2005. Numerical simulation of fatigue-driven delamination using interface elements. Int. J. Numer. Meth. Eng. 63, 1824–1848.

Rühle, M., 2004. Struktur und chemische Zusammensetzung von inneren Grenzflächen in verschiedenen Materialien. Tätigkeitsbericht, Max-Planck-Institut für Metallforschung, Stuttgart, pp. 429–437.

Schaumburg, H., 1994. Werkstoffe und Bauelemente der Elektrotechnik Band 2: Keramik. Teubner.

Schellekens, J., De Borst, R., 1993. On the numerical integration of interface elements. Int. J. Numer. Meth. Eng. 36, 43–66.

Schorn, P., Bräuhaus, D., Böttger, U., Waser, R., Beitel, G., Nagel, N., Bruchhaus, R., 2006. Fatigue effect in ferroelectric $PbZr_{1-x}Ti_xO_3$ thin films. J. Appl. Phys. 99, 1141041–1141045.

Schröder, J., Gross, D., 2004. Invariant formulation of the electromechanical enthalpy function of transversely piezoelectric materials. Arch. Appl. Mech. 73, 533–552.

Schröder, J., Romanowski, H., 2005. A thermodynamically consistent mesoscopic model for transversely isotropic ferroelectric ceramics in a coordinate-invariant setting. Arch. Appl. Mech. 74, 863–877.

Serebrinsky, S., Ortiz, M., 2005. A hysteretic cohesive-law of fatigue-crack nucleation. Scripta Mater. 53, 1193–1196.

Sfantos, G., Aliabadi, M., 2007. A boundary cohesive grain element formulation for modelling intergranular microfracture in polycrystalline brittle materials. Int. J. Numer. Meth. Eng. 69, 1590–1626.

Smith, R.C., 2005. Smart material systems, SIAM. Front. Appl. Math. 7.

Utzinger, J., Bos, M., Floeck, M., Menzel, A., Kuhl, E., Renz, R., Friedrich, K., Schlarb, A., Steinmann, P., 2007a. Computational modelling of thermal impact welded peek/steel single lap tensile specimens. Comput. Mater. Sci. 41, 287–296.

Utzinger, J., Menzel, A., Steinmann, P., Benallal, A., 2007b. Aspects of bifurcation in an isotropic elastic continuum with orthotropic inelastic interface. Euro. J. Mech. A Solids. doi:10.1016/j.euromechsol.2007.11.001.

Westram, I., Oates, W., Lupascu, D., Rödel, J., Lynch, C., 2007. Mechanism of electric fatigue crack growth in lead zirconate titanate. Acta Mater. 55, 301–312.

Willam, K., Rhee, I., Shing, B., 2004. Interface damage model for thermomechanical degradation of heterogeneous materials. Comput. Meth. Appl. Mech. Eng. 193, 3327–3350.